Peering Inside Tropical Cyclones With the WIVERN SpaceBorne Doppler Radar

AGU ADVANCING EARTH AND SPACE SCIENCES

Earth and Space Science

RESEARCH ARTICLE
10.1029/2025EA004680

Peering Inside Tropical Cyclones With the WIVERN Space-Borne Doppler Radar

Alessandro Battaglia[1,2], Francesco Manconi[1], Massimiliano Recupero[1], Cinzia Cambiotti[1], Marco Coppola[1], Antonio Parodi[3], Frederic Tridon[1], Simone Mantovani[4], Pavlos Kollias[5,6], David S. Nolan[7], Marcel Kleinherenbrink[8], and Maryam Pourshamsi[8]

[1]Dipartimento di Ingegneria dell'Ambiente, del Territorio, Politecnico di Torino, Turin, Italy, [2]Department of Physics and Astronomy, University of Leicester, Leicester, UK, [3]CIMA Foundation, Savona, Italy, [4]MEEO, Ferrara, Italy, [5]School of Marine and Atmospheric Sciences, Stony Brook University, NY, USA, [6]Department of Atmospheric and Oceanic Sciences, McGill University, Montreal, QC, Canada, [7]Department of Atmospheric Sciences, Rosenstiel School of Marine and Atmospheric Science, University of Miami, Miami, FL, USA, [8]European Space Agency, Noordwijk, The Netherlands

Key Points:

- The WIVERN mission concept aims to provide three-dimensional profiles of in-cloud winds and cloud structure across scales from 1 to 1,000 km using its unique Doppler radar capabilities
- WIVERN can provide three-dimensional views of the horizontal wind and ice mass inside tropical cyclones, capturing the vertical wind shear and regions of wind convergence and divergence, thus revealing the mechanisms behind its formation
- WIVERN can estimate the maximum winds in the inner core when multiple close-in-time overpasses are available, thereby capturing the intensification of a tropical cyclone

Correspondence to:
A. Battaglia,
alessandro.battaglia@polito.it

Citation:
Battaglia, A., Manconi, F., Recupero, M., Cambiotti, C., Coppola, M., Parodi, A., et al. (2026). Peering inside tropical cyclones with the WIVERN space-borne Doppler radar. *Earth and Space Science*, *13*, e2025EA004680. https://doi.org/10.1029/2025EA004680

Received 4 SEP 2025
Accepted 7 MAR 2026

Author Contributions:
Conceptualization: Alessandro Battaglia, Antonio Parodi
Data curation: Alessandro Battaglia, Francesco Manconi, Massimiliano Recupero, Cinzia Cambiotti, Antonio Parodi
Formal analysis: Alessandro Battaglia, Francesco Manconi, Massimiliano Recupero, Cinzia Cambiotti, Marco Coppola, Antonio Parodi
Funding acquisition: Alessandro Battaglia
Investigation: Alessandro Battaglia, Francesco Manconi, Marco Coppola, David S. Nolan, Marcel Kleinherenbrink

Abstract The WIVERN (Wind Velocity Radar Nephoscope) mission significantly enhances the global tropical cyclone observing system. Operating from a 500 km near-polar orbit, the 3 m diameter conically scanning antenna provides an 800 km swath. The radar operated at 94 GHz (3 mm wavelength) provides high-resolution observations with a vertical resolution of 600 m and horizontal resolution finer than 1 km. With quasi-daily global coverage, WIVERN measures in-cloud tropical cyclone winds from 1 km above the surface to the upper troposphere. Simulations of the Weather Research and Forecasting model with 1.5 km grid spacing were carried out for Hurricane Milton (2024) to serve as a testbed to demonstrate the potential capabilities of the WIVERN mission and its associated data products. The high-resolution simulation successfully reproduces the hurricane's trajectory and intensification, capturing a remarkable 78-knot increase in maximum sustained wind speed during the 24-hr period from 7 October to 8 October. End-to-end simulations demonstrate that WIVERN: (a) can provide a three-dimensional view of the horizontal wind inside cyclones, in particular capturing the vertical wind shear, the upper level divergence and the in-cloud circulations inside the anvil produced by the hurricane convective towers, and some of the inflow and outflows in the lower layers of the atmosphere; (b) in presence of close-in-time overpasses, has the potential to detect the intensification of cyclone by estimating the maximum winds in the inner core; (c) can profile the tropical cyclone ice mass as a function of the distance from the eye, which will help shed light on the anvil formation and dissipation mechanisms.

Plain Language Summary WIVERN, the mission selected by ESA as the Earth Explorer 11, is designed to provide novel global observations of storms. It uses a radar in a near-polar orbit to scan wide areas (800 km swath) with high detail-600 m vertically and less than 1 km horizontally. WIVERN provides nearly daily coverage and measures wind inside clouds from near the surface to high altitudes. Simulations tailored to tropical cyclones show that WIVERN has ground-breaking potential for: (a) providing 3D wind data inside cyclones, including wind shear, cloud circulation, and inflows/outflows. (b) Detecting cyclone intensification by measuring maximum winds when the satellite passes closely over the storm. (c) Measuring ice mass in the cyclone, helping understand how the storm's anvil forms and dissipates.

1. Introduction

According to the US National Hurricane Center a Tropical Cyclone (TC) is "a warm-core non-frontal synoptic-scale cyclone, originating over tropical or subtropical waters, with organized deep convection and a closed surface wind circulation about a well-defined center" with peak wind speeds exceeding 50 ms^{-1} in severe TCs (hurricanes and typhoons). They play a significant role in the Earth's radiation budget and in the water cycle by transporting heat and moisture from the tropics to the mid-latitudes and by releasing large quantities of latent heat (Emanuel, 2001, 2003; Scoccimarro et al., 2011). In addition to their climatic significance, TCs pose severe societal risks, causing extensive damage due to strong winds, torrential rainfall, and flooding upon landfall (Klotzbach et al., 2018). Moreover, storm surge generated by the TC core can propagate far from the storm, further impacting coastal regions (Yurovskaya et al., 2023). Once formed, tropical cyclones can undergo rapid intensification (i.e., an increase in maximum sustained winds of at least 15 m/s within 24 hr), reaching fully destructive intensity within just 1 to 2 days (Kaplan & DeMaria, 2003).

Methodology: Alessandro Battaglia, Cinzia Cambiotti, Marco Coppola, David S. Nolan
Project administration: Alessandro Battaglia
Software: Massimiliano Recupero
Supervision: Alessandro Battaglia
Validation: Alessandro Battaglia
Visualization: Massimiliano Recupero, Cinzia Cambiotti, Marco Coppola, Antonio Parodi, Simone Mantovani
Writing – original draft: Alessandro Battaglia, David S. Nolan
Writing – review & editing: Alessandro Battaglia, Francesco Manconi, Massimiliano Recupero, Cinzia Cambiotti, Marco Coppola, Antonio Parodi, Frederic Tridon, Pavlos Kollias, David S. Nolan, Marcel Kleinherenbrink, Maryam Pourshamsi

Tropical cyclogenesis is an upscaling process whereby convective-scale dynamics locally add energy and vorticity to a large-scale cyclonic disturbance in regions where synoptic conditions are conducive to convective development. There is still no broad consensus on how to understand and predict tropical cyclogenesis (Emanuel, 2018). Several studies have found that environmental vertical wind shear (usually defined in the environment surrounding the TC between 200 and 850 hPa) is the main inhibitor of tropical cyclogenesis, intensification and dissipation, due to its ability to induce kinematic and thermodynamic asymmetry (Nolan & Rappin, 2008; Rios-Berrios et al., 2024; Schenkel et al., 2020; Thatcher & Pu, 2011; Wadler et al., 2022, and references therein). In this context, low vertical shear allows for a vertically aligned vortex, maintaining the coherence between the lower and upper tropospheric circulation. This alignment is essential for sustaining deep convection near the storm center and fostering a symmetric inner-core structure, which facilitates efficient latent heat release and intensification processes. On the other hand, moderate to strong shear can tilt the vortex, displace convection from the center, and disrupt the upper-level outflow, ultimately suppressing intensification or even causing weakening (Frank & Ritchie, 2001). In addition, strong vertical wind shear tends to result in dry air entrainment which is detrimental to TC genesis.

However, TC intensity change is generally governed by more complex, intertwined, multi-scale processes (Judt & Chen, 2016). The prediction of TC rapid intensification and the mechanisms controlling this process remain areas of active research; e.g., Y. Liu et al. (2025) recently suggested that the size of the TC has a significant impact on its intensification; likewise Ou et al. (2025) revealed distinct outflow dynamics and cloud properties differentiating rapid intensification from slow-intensifying TCs. The environmental effects that govern the evolution of TC intensity (e.g., ambient humidity, sea surface temperature, ocean mixed layer depth and wind shear) have been thoroughly discussed in the literature and their respective contribution are still the subject of debate (see, e.g., Emanuel et al., 2004; Hendricks et al., 2010; Wang et al., 2025). Conversely, internal dynamical processes such as convective bursts and eyewall formation can be key drivers in TC intensification, but are not well understood (Rogers et al., 2013; Wu et al., 2016). Based on a database of more than 8,000 high-resolution CloudSat Cloud Profiling Radar (CPR) overpasses of TCs (Tourville et al., 2015) and by exploiting the fact that the Ice Water Content (IWC) derived from cloud spaceborne radars such as CloudSat or EarthCARE CPR can be used as a proxy for latent heating, S.-N. Wu and Soden (2017) have demonstrated that strengthening storms have 20% higher IWC than weakening storms, especially in the midtroposphere near the eyewall (see their Figure 2). Since rapid intensification is often associated with the reorganization of the TC mesoscale cloud and precipitation structures, it is essential that models are able to predict such structures accurately and for the right physical and dynamical reasons.

The description of the secondary circulation of a mature TC also remains a topic of study. Several foundational studies suggest that it consists of a boundary layer inflow that first rises in the deep convective towers of the eyewall before turning outward to form the cirrus cloud shield just below the tropopause (Houze, 2010). In this widely accepted view, updrafts within the outer rainbands are not contributing to the primary outflow (see Figure 1 in Nolan et al. (2025)). Novel TC simulations performed by Nolan et al. (2025) reveal a different picture from the examination of the mass and moisture budgets of the cirrus outflow shield: a significant fraction of the dry air mass flux (widely varying but around 50%) and even larger fraction of the condensate in the outflow is supplied by deep convection in the surrounding rain-bands (see Figure 8 in Nolan et al. (2025)). This pinpoints at the importance of the rainband convection in controlling the size and thickness of the outflow clouds, which is a key feature for estimating storm intensity.

In recent years, significant progress has been made in the monitoring of TCs from space and such advancements will continue in the upcoming years (Ricciardulli et al., 2023). While in situ and aircraft remote sensing data allow dense monitoring of TCs in the Atlantic Ocean (Holbach et al., 2023), satellite observations remain essential in the other basins and away from the coasts in the Atlantic. In brief, spaceborne observations include:

- Synthetic Aperture Radar (SAR) systems, capable of mapping surface winds at km-scale resolution without suffering from high wind or rain-induced saturation and of capturing features such as the eyewall (and its circulation), outflow boundaries, and rainbands (e.g., Avenas et al., 2023; Mouche et al., 2019);
- C and K_u-band scatterometers and radiometer systems with frequency bands from *L* to *X* (e.g., SMOS, SMAP, AMSR-2) providing winds at the surface but at coarser resolutions, TC center location, intensity, radial and rotational structure. The new generation of scatterometers with cross polarization will improve measurements for extreme hurricane winds;

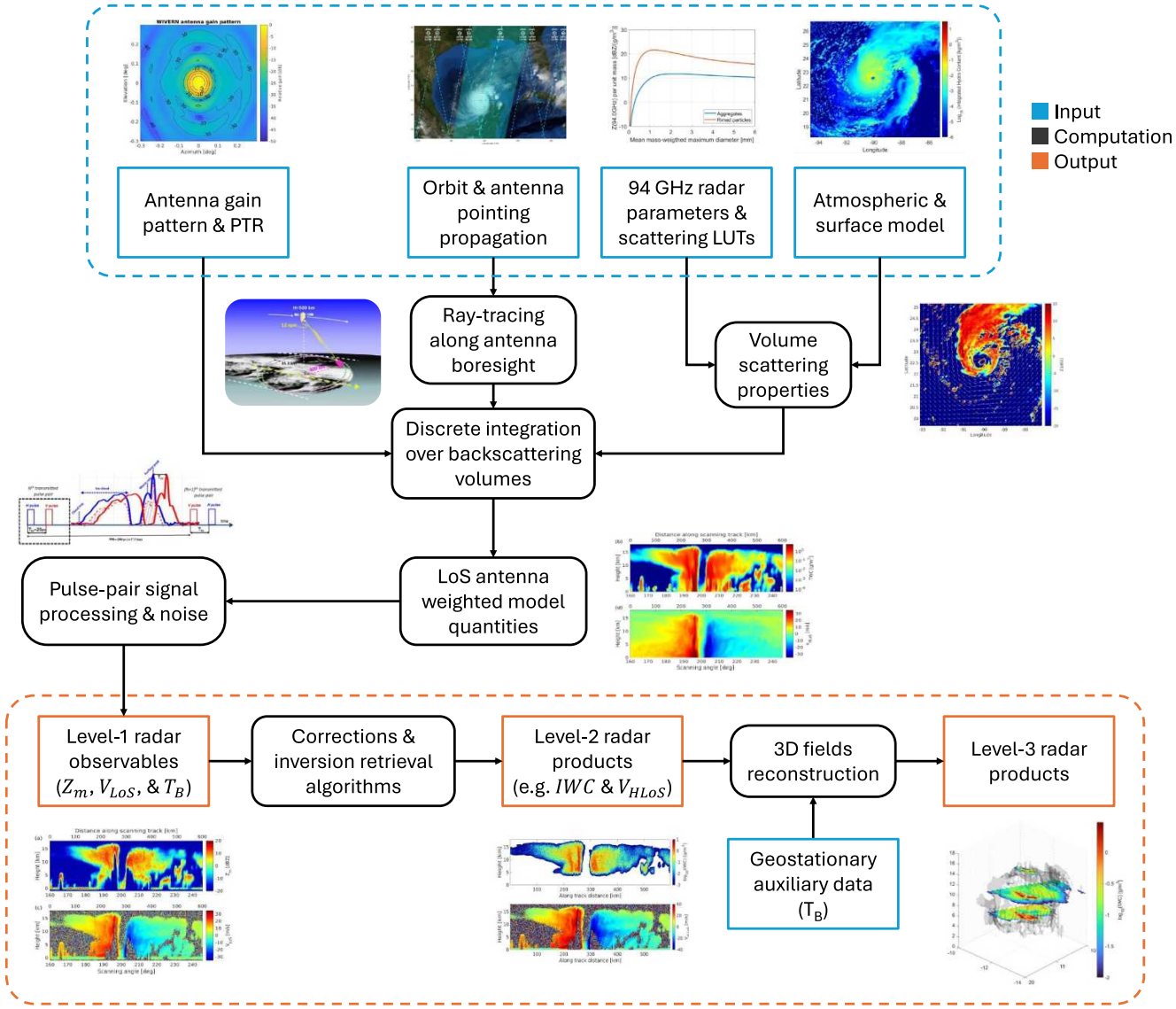

Figure 1. Flow chart of the WIVERN mission end-to-end simulator architecture.

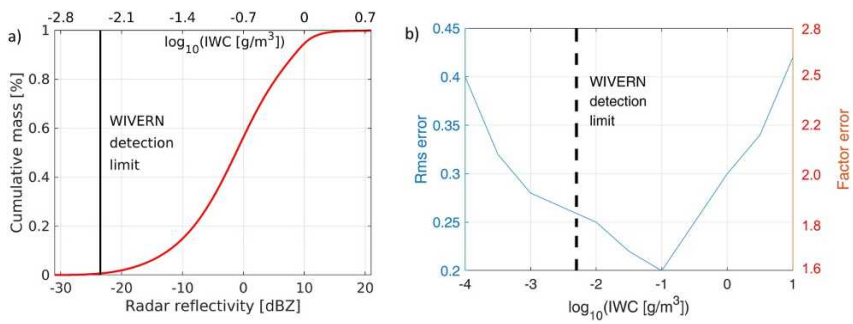

Figure 2. Left panel: cumulative mass for ice clouds as a function of the radar reflectivity factor as computed from the CloudSat 2B-CWC-RO IWC product for the entire year 2008. Right panel: root mean square error for $\log_{10}(IWC[g/\mathrm{m}^3])$ according to Protat et al. (2007) as a function of the IWC (in log-units).

Figure 3. WRF domains at 4.5 and 1.5 km grid spacing.

- Microwave imagers/sounders (e.g., GMI, SSMIS and, in the future, CIMR and MWI) providing, in addition to surface properties (wind speed and sea surface temperatures), information about precipitation, water vapor and cloud contents (but with very coarse vertical resolution). This also includes a new generation of small and cube satellites (e.g., TROPICS and TEMPEST);
- Doppler wind LiDARS with ESA-Aeolus2 expected to fly in the next decade after Aeolus demonstrated the potential of spaceborne Doppler LiDAR for observing clear air dynamics around the cyclones.
- Geostationary sensors monitoring the rapid temporal evolution of convective features and exact location of the storm and producing atmospheric motion vectors for storm cloud tops. Resolutions down to 1–2 min will soon become operational for targeted areas.

K_u-K_a-W band spaceborne radars (Battaglia et al. (2020) and references therein) have been particularly useful for profiling cloud and precipitation inside tropical cyclones.

- The TRMM with its K_u band radar and then GPM mission with its K_u-K_a band radars have provided unique insight in the microphysical structures and processes of TC precipitation for example, by identifying the relevance and relative importance of processes like collision-coalescence, evaporation and breakup (Huang & Chen, 2019; Porcacchia et al., 2019). These observations can also identify the vertical evolution of raindrop size distribution, ice microphysics and latent heat as a function of different precipitation rates and efficiencies, and characterize how the vertical structure changes in stratiform versus convective areas, in various parts of

the TC (namely the eyewall and the inner and outer regions) or in different shear-relative quadrants and/or ocean basins (Brauer et al., 2024; Cecil et al., 2002; Hence & Houze, 2011, 2012; Uma & Reshma, 2024; Zagrodnik & Jiang, 2014).

- Thanks to their high sensitivity, the EarthCARE and CloudSat W-band cloud profiling radars offer unprecedented information on the vertical structure of clouds (cloud type, ice water contents, radiative heating rates) (Lee & Wing, 2024; Subrahmanyam et al., 2018; Tourville et al., 2015; S.-N. Wu et al., 2020, 2021), albeit with limited coverage due to their nadir-looking observation geometry. The increased sensitivity of W-band radars compared to Ku and Ka radars is particularly effective in mapping the glaciated part of the clouds as demonstrated by coincident CloudSat and GPM overpasses (Turk et al., 2021).

Despite this plethora of instruments, there is a lack of simultaneous observations of the three-dimensional structure of the winds and of the hydrometeors inside TCs. The Wind Velocity Radar Nephoscope (WIVERN) mission, equipped with a groundbreaking Doppler radar (Battaglia, Rizik, et al., 2025; ESA WIVERN Team, 2025; Illingworth et al., 2018), promises to fill this gap in the observing system and capture, for the first time, the three-dimensional dynamics and microphysical structure of all types of storms on Earth below 86° latitude. This includes horizontal winds in stratiform regions, updrafts and downdrafts in convective cells, and the mass of condensed water above the freezing level. The mission will cover a more than 800 km wide swath with quasi-daily revisit times. WIVERN measurements will be collected at 1 km intervals along its conically scanning beam and will be vertically resolved with a resolution of 600 m.

This work aims at demonstrating that the WIVERN mission will achieve two major goals. First, WIVERN will provide in-cloud wind measurements, thus bridging the observational gap between the surface (as provided by SARs, scatterometers and radiometers) and the upper troposphere winds (as provided by geostationary sensors). For each overpass, in less than two minutes, the WIVERN Doppler radar will provide a full three-dimensional map of horizontal winds within TCs where clouds exceeding −18 dBZ are present. The number of profiles collected by WIVERN in a single overpass inside the TC will be equivalent to that acquired by a research aircraft equipped with a nadir-looking radar sampling continuously for about 2–3 days. Second, WIVERN will simultaneously provide a unique, three-dimensional view of clouds and precipitation across the entire storm, complementing in the TC glaciated part that TRMM and GPM K_u and K_a band precipitation radars have provided inside moderate and heavy precipitation regions (Battaglia et al., 2020).

The theory underpinning the concept is outlined in Section 2. Then simulations of WIVERN overpasses are thoroughly discussed (Section 3). Conclusions and recommendations are drawn in Section 4.

2. Methodology

The WIVERN radar operates from a 500 km near-polar orbit with a 3 m diameter conically scanning antenna with pointing off-nadir, leading to an incidence angle of approximately 42°. This configuration provides coverage across an 800 km swath, with vertical resolution of 600 m, and horizontal resolution of approximately 1 km. With quasi-daily global coverage, WIVERN will enable the measurements of in-cloud TC winds from ≈ 1 km above the surface (due to clutter contamination, Coppola et al., 2025) to the upper troposphere, spanning horizontal scales from 1 to 800 km.

Throughout ESA studies, a comprehensive end-to-end simulator was developed to reproduce WIVERN observables from atmospheric and surface targets, incorporating successive refinements (Battaglia, Rizik, et al., 2025; Manconi et al., 2025; Rizik et al., 2023) to the initial framework proposed in Battaglia et al. (2022). The schematic of Figure 2 illustrates the main steps, inputs and outputs of the simulator.

In brief, the simulator uses outputs from cloud-resolving models, such as the Weather Research and Forecasting Model (WRF, Skamarock et al., 2019; Powers et al., 2017), which provide three-dimensional distributions of wind, hydrometeors, temperature, and water vapor (see Section 2.1). These quantities are then converted into 94 GHz radar properties, or stimuli, including extinction, scattering, backscattering coefficients, single scattering albedo, and asymmetry factors via 94 GHz scattering look-up tables that are pre-computed (details in Battaglia et al. (2022)). Similarly the terminal velocities are computed as a function of the particle maximum dimension D using:

- For rain and cloud the parametrization adopted by Tridon and Battaglia (2015);
- For snow $V_T = 0.69\, D^{0.21}$ with D in mm;

- For graupel: $V_T = 0.86\, D^{0.87}$ with D in mm.

The terminal velocities are then weighted by the backscattering cross section to compute the Doppler (reflectivity-weighted) sedimentation velocities, V_T^D.

Each footprint is illuminated by the WIVERN antenna and scanning pattern for any given orbit, computing the Level 1 radar observables [line-of sight (LoS) Doppler velocity (V_{LoS}), radar reflectivity factor (Z) and brightness temperatures in the H- and V-polarized channels ($T_b^{H,V}$)] taking into account the sampling rate, the sensitivity and the specific pulse scheme of the instrument (details in Battaglia, Rizik, et al. (2025)). Section 2.2 discusses how the simulations are set up and provides an example of the outputs.

From the Level-1 radar observables a variety of Level-2 products can be derived (ESA WIVERN Team, 2025). Here, the focus is restricted to the Horizontal wind along the horizontally projected Line of Sight (HLoS) and the IWC. Before any estimate of Level-2 products can be made, several corrections are applied to the reflectivity and LoS Doppler velocity fields.

The simulated radar return signals are first noise subtracted and then the reflectivity is estimated similar to what is done for CloudSat and EarthCARE (Kollias et al., 2023; Marchand et al., 2008). The reflectivities are then corrected for gaseous attenuation using the model fields of vapor, temperature and pressure profiles. WIVERN transmits two pulses in two orthogonal polarizations closely separated in time. The received echoes are therefore overlapping in time so that cross-pol returns from one transmission cause contamination in the other. These spurious signals can be eliminated in post-processing (Rizik et al., 2023). Finally, the range bins contaminated by surface clutter echoes are filtered out (Coppola et al., 2025; Manconi et al., 2025).

Biases in the LoS Doppler velocity due to non-uniform beam filling and wind shear inside the radar volume are corrected by using gradients of the reflectivity and of the velocity fields (Battaglia, Rabino, et al., 2025). The two dimensional spatial variability of the reflectivity and Doppler velocity fields together with the brightness temperatures are used as input to identify, via a U-NET based neural network, "convective" regions where vertical velocities (indicated with w) exceed $|w| > 1$ m/s (Mustich et al., 2025). The machine learning methodology has been trained on a vast data set of simulation by using the model vertical velocities as truth.

The HLoS Velocity (V_{HLoS}) product is then computed in stratiform regions where vertical winds can be neglected ($|w| < 1$ m/s). Then, V_{HLoS} is computed from trigonometry as:

$$V_{HLoS} = \frac{V_{LoS} - \left(\cancel{w} + V_T^D\right)\cos(\theta_I)}{\sin(\theta_I)} \approx 1.5\, V_{LoS} - 1.1\, V_T^D \tag{1}$$

where $\theta_I \approx 42°$ is the WIVERN beam incidence angle, V_{LoS} is the measured LoS velocity (corrected for mis-pointing and non uniform beam filling effects, Battaglia, Rabino et al., 2025; Scarsi et al., 2024).

Above the freezing level in ice V_T^D can be derived by empirical relationships of the form $V_T^D = f(Z,T)$, all based on surface-based vertically pointing Doppler radars (Kalesse & Kollias, 2013; Protat & Williams, 2011). The statistical distribution shows that, for ice crystals the observed relationship is linear with reflectivity (ESA WIVERN Team, 2025, e.g. $V_T^D = 0.88 + 0.0082\, Z\left[\mathrm{mm^6/m^3}\right]$ for $-25°\mathrm{C} \le T < -20°\mathrm{C}$) when considering different temperature ranges, with the most representative vertical velocity close to 1 m s^{-1}. Viceversa the Doppler terminal velocity of raindrops can be inferred from rain rate according to disdrometer observations (e.g., a relationship of the form $V_T^D = 3.9\, RR[\mathrm{mm/h}]^{0.067}$ can be used). It typically varies only between 3 and 5 m s^{-1}. In between, V_T^D of melting hydrometeors can be linearly interpolated. The spread in terminal velocities of ice crystals and rain results in a residual error in V_{HLoS} winds of less than 1 m s^{-1}.

Established Z-IWC uncertainties (Protat et al., 2007) are adopted to characterize the error structure of the IWC retrieval for each WIVERN ray associated to the inversion from Z to IWC, under the assumption the overall retrieval is unbiased. With WIVERN expected sensitivity of about −23.5 dBZ at 1 km integration (ESA WIVERN Team, 2025), an IWC detection limit of about 0.005 g/m^3 is foreseen (the relationship $Z = 0.198\, Z^{0.7}$ valid for tropical ice clouds from Protat et al. (2007) is adopted). Note that this limit accounts for 99.3% of the mass of ice clouds (see left panel in Figure 2) as computed by using CloudSat 2B-CWC-RO IWC product statistics for the

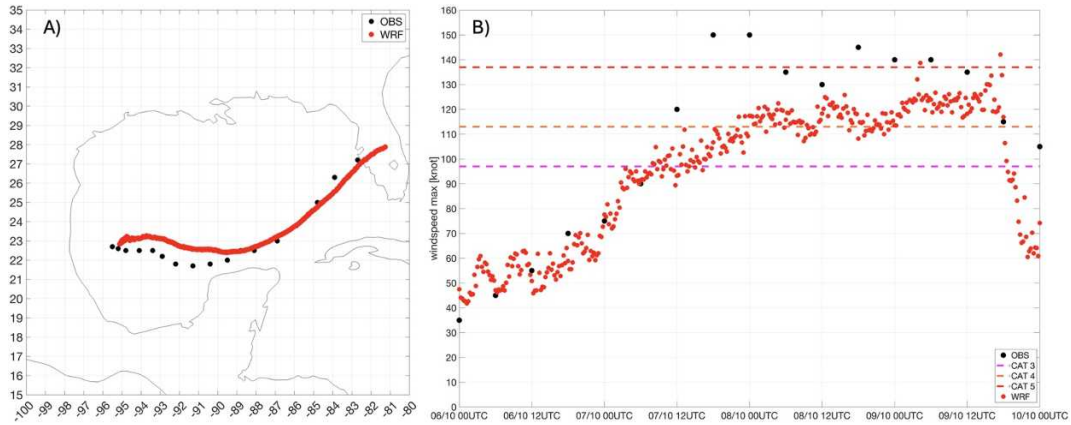

Figure 4. Panel (a): comparison between the NHC best track (6 hourly data) and the WRF model vortex track with 15 min time resolution. Panel (b): comparison between the NHC maximum wind speed (6 hourly data) and the WRF model instantaneous maximum wind speed with 15 min time resolution.

entire 2008. No retrieval is attempted in convective columns, identified by model vertical winds that exceed in absolute value 2 m/s.

The retrieval error is dominated by the uncertainties associated with translating the radar backscattering signal into the IWC geophysical parameter. Following the findings by Protat et al. (2007) for a 94 GHz radar operating in the tropics, the noise function reproduced in the right panel of Figure 2 for the $\log_{10}(IWC)$ is used to inject noisiness into the retrieval. This root-mean-square (rms) error of the $\log_{10}(IWC)$ corresponds to a multiplicative error for the IWC with a factor, $f \equiv 10^{rms}$, indicated on the right y-axis. Consequently, for each WIVERN backscattering volume, IWC is sampled from a log-normal distribution, whose mean value, $\langle IWC \rangle$, corresponds to the value derived via the Z-IWC and the standard deviation is computed as half the difference $f\langle IWC \rangle - \langle IWC \rangle / f$.

From these two Level-2 products (horizontal LoS wind and ice mass) which are defined along the WIVERN rays (and therefore represent a cloud of sparse points across the TC volume), Level-3 three-dimensional gridded fields can be reconstructed, following the methods explained in Sections 2.4 and 2.5.

2.1. WRF Simulations of Hurricane Milton

2.1.1. Overview of Hurricane Milton

Hurricane Milton was an extraordinarily powerful Atlantic hurricane that originated on 5 October 2024 in the southwestern Gulf of Mexico. Over the subsequent 2 days, it experienced explosive intensification, escalating from a tropical depression to Category 5 by 7 October, with sustained winds reaching 180 mph (approximately 285 km/hr) and a minimum central pressure of 895 hPa, rendering it one of the most intense hurricanes ever documented in the Atlantic basin. Following its peak, Milton experienced a slight weakening due to an eyewall replacement cycle, but subsequently re-intensified to Category 5, before gradually diminishing again as it progressed northeast toward Florida, where it encountered cooler waters and increasing wind shear. On the morning of 9 October 2024, the storm made landfall near Siesta Key, Florida, as a Category 3 hurricane with winds around 120 mph (approximately 193 km/hr). The impacts were severe: the storm surge reached 2.5–3 m in certain coastal areas, heavy rainfall and flooding affected much of central Florida, resulting in widespread power outages, significant property and infrastructure damage, and large-scale disruption to agriculture and communities. The rapid development, remarkable strength, and devastating aftermath of Hurricane Milton establish it as one of the most extreme hurricanes in recent Atlantic history.

2.1.2. WRF Set-Up

In this study WRF model version 4.6.1 has been adopted with 2 two-way nested domains at 4.5, and 1.5 km grid spacing (Figure 3).

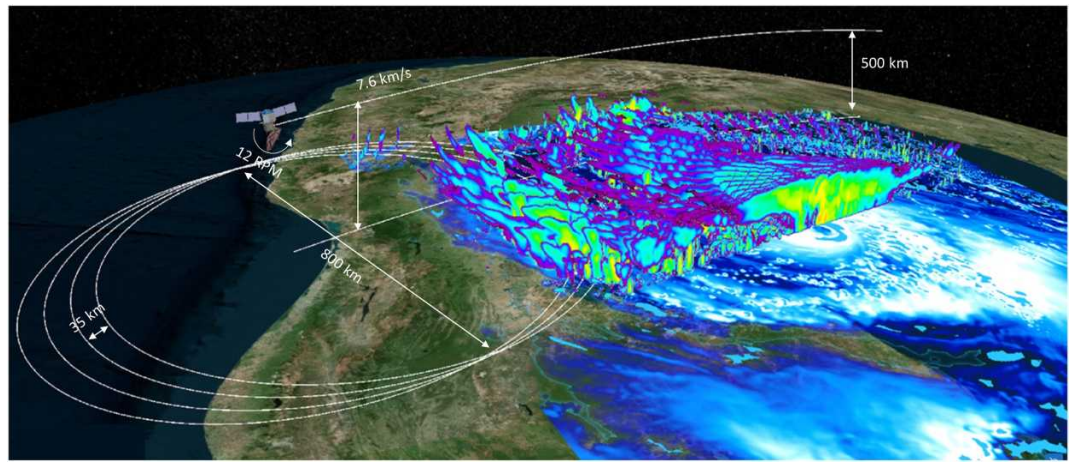

Figure 5. Illustration of the scanning geometry envisioned for the WIVERN mission. For representation purposes, dimensions are not to scale. The right edge of WIVERN swath is just crossing the hurricane eye. The Level-1 reflectivity product is illustrated across WIVERN swath whereas the total hydrometeor content field is depicted with bluish colors (white indicate high contents, dark blue small contents) on the easternmost part of the hurricane, outside WIVERN swath.

The innermost domain at 1.5 km grid spacing is based on the WRF model moving-nest approach (Gill et al., 2004). This option allows one of the nested domains to follow a feature of interest, such as a tropical cyclone, convective system, or any other moving weather phenomenon. This enables higher-resolution modeling in the area of interest throughout the simulation, conserving computational resources while improving forecast accuracy in critical regions. The initial and boundary conditions are provided by ERA5. The ERA5 data set is a cutting-edge global climate reanalysis product developed by the ECMWF as part of the Copernicus Climate Change Service (C3S). It represents the fifth generation of ECMWF reanalysis efforts, succeeding the ERA-Interim data set. ERA5 features significant enhancements compared to ERA-Interim, including improved spatial and temporal resolution, with a grid resolution of around 31 km and a temporal resolution of 1 hr (Hersbach et al., 2020; Soci et al., 2024). ERA5 provides comprehensive data coverage from 1940 to the present, with updates occurring every 2 months.

The WRF model study simulation is initialized on 5 October 2024 and it runs until 11 October 2024 with 6 hourly boundary conditions provided by ERA5 analysis. Concerning the WRF model setup, the Rapid Radiative Transfer Model for GCMs (RRTMG) shortwave and longwave schemes (Iacono et al., 2008) are used for radiation, while the Rapid Update Cycle (RUC) scheme is chosen as a multi-level soil model (6 levels) with higher resolution in the upper soil layer (Benjamin et al., 2004; Smirnova et al., 1997, 2000). No cumulus scheme is activated in the two domains (4.5 and 1.5 km grid-spacing), because convection can be resolved explicitly on both grids. The microphysics is simulated using Thompson hail/graupel/aerosol aware scheme (Thompson & Eidhammer, 2014) which includes ice, snow, graupel and hail processes suitable for high-resolution simulations, considers water- and ice-friendly aerosols. Aerosol-ice friendly aerosols are atmospheric particles that are capable of initiating the formation of ice crystals in supercooled cloud droplets (i.e., droplets that remain liquid below 0°C). These aerosols promote heterogeneous ice nucleation, a process important in cloud microphysics and climate modeling. This microphysics computes two-moment prognostics (water content and number concentration) for graupel and hail, including a predicted density graupel category. In terms of turbulence closure, the turbulent mixing is operated by the 1.5-order turbulent kinetic energy (TKE) prediction in line with previous km-scale studies (Fiori et al., 2010, 2011, 2017; Lagasio et al., 2022).

2.1.3. WRF Results

The model's performance to realistically simulate Hurricane Milton is assessed by examining its ability to reproduce the observed track and intensity evolution, as documented by the National Hurricane Center (NHC).

Figure 4 presents a comparison between the National Hurricane Center (NHC) best track data, provided at 6-hr intervals, and the WRF-simulated track, output at 15-min intervals, for the period spanning 00 UTC on 6 October

to 00 UTC on 10 October 2024. The overall agreement between the two tracks is very good, although the simulated landfall occurs approximately six hours earlier than observed.

The WRF model is recognized for experiencing issues related to the interaction between numerical dissipation and the rapid intensification of hurricanes, as elaborated in the study by Hasan et al. (2022). This phenomenon arises because the pressure gradient discretization in WRF is limited to second order, which leads to a smoothing effect on the response to localized heating anomalies that are linked to convective bursts. Consequently, this results in the simulation of hurricanes that are weaker than what is observed and, as a result, moving at a faster pace than the actual trajectory. To mitigate this issue, the simulation was adjusted by decreasing the TKE coefficient to 12.5% of its default value, namely $c_k = 0.15$, where the TKE coefficient relates turbulent fluxes to TKE and stability of the atmosphere. This adjustment facilitated a more accurate representation of the Milton Hurricane regarding both its tracking and intensity.

In terms of storm intensity, the WRF model also performs well, capturing the period of rapid intensification (RI) between 12 UTC on 6 October and 00 UTC on 8 October 2024. It is noteworthy that while the observed Hurricane Milton reached Category 5 intensity, the WRF simulation peaked at Category 4. Despite this slight underestimation, the strong consistency in both trajectory and intensity evolution provides confidence in the use of this simulation as a realistic testbed for evaluating WIVERN performance and retrieval capabilities.

2.2. WIVERN Doppler Radar Simulations

WIVERN radar simulations are performed using output from the WRF model simulation of Hurricane Milton, covering the period from 10:00 UTC on 6 October 2024 to 00:00 UTC on 8 October 2024, with a temporal resolution of 1 hr, resulting in a total of 39 hourly snapshots. For each time step, the simulator ingests a three-dimensional domain of 1,250 × 1,250 × 20 km^3 centered on the hurricane's eye. The data are interpolated onto a grid with a horizontal resolution of approximately 1.5 km and vertical resolution of approximately 500 m with finer vertical spacing below 3 km to better resolve low-level features such as the boundary layer and near-surface wind structures.

The orbit and antenna pointing geometry of WIVERN are propagated over the full 39-hr duration of the available WRF simulation for Hurricane Milton. The simulation uses realistic orbital parameters corresponding to the planned sun-synchronous orbit of WIVERN, including an inclination of 97.4°, an altitude of approximately 500 km, and a Local Time of Ascending Node (LTAN) of 6 a.m.

During the propagation period, any satellite overpass for which the ground track passes within 400 km of the hurricane eye is registered as a valid overpass and selected for further radar simulation. For each valid overpass, a 200-s simulation window is centered on the time of minimum distance between the satellite ground track and the cyclone center. This corresponds to approximately 40 complete rotations of the conically scanning radar antenna and ensures realistic sampling of the hurricane structure under the WIVERN observing geometry.

During the 40 antenna rotations, the satellite advances approximately 1,400 km along its ground track, enabling complete coverage of the hurricane with both the forward- and backward-looking views of WIVERN's scanning geometry (see Figure 5). An illustration of the simulation setup is shown in Figure 6, while an example of the resulting radar cross-sections is presented in Figure 7.

Figure 6 illustrates a sequence of WIVERN satellite overpasses across the path of Hurricane Milton, covering the period from 5 to 10 October 2024. During this time, Milton originated as a tropical storm in the western Gulf of Mexico and underwent rapid intensification, transitioning from Category 2 to Category 5 within a single day on 7 October, before making landfall in Florida as a Category 3 hurricane.

The dashed cyan lines in Figure 6 represent the simulated WIVERN ground tracks over the Gulf of Mexico region, based on the realistic orbital parameters planned for the mission. Out of the 10 overpasses shown, five tracks pass within 400 km of the hurricane eye, allowing for sampling of at least half of the storm structure during each pass. These five key overpasses are marked with numbered squares and diamonds, indicating the positions of minimum distance between the satellite ground track and the TC eye, respectively.

Of particular interest in this study are overpasses (2 and 3) (thick dashed lines), which are separated by only 24 hr and capture the cyclone across its rapid intensification phase, offering valuable opportunities to evaluate WIVERN's capability in observing storm dynamics during this critical period.

10.1029/2025EA004680

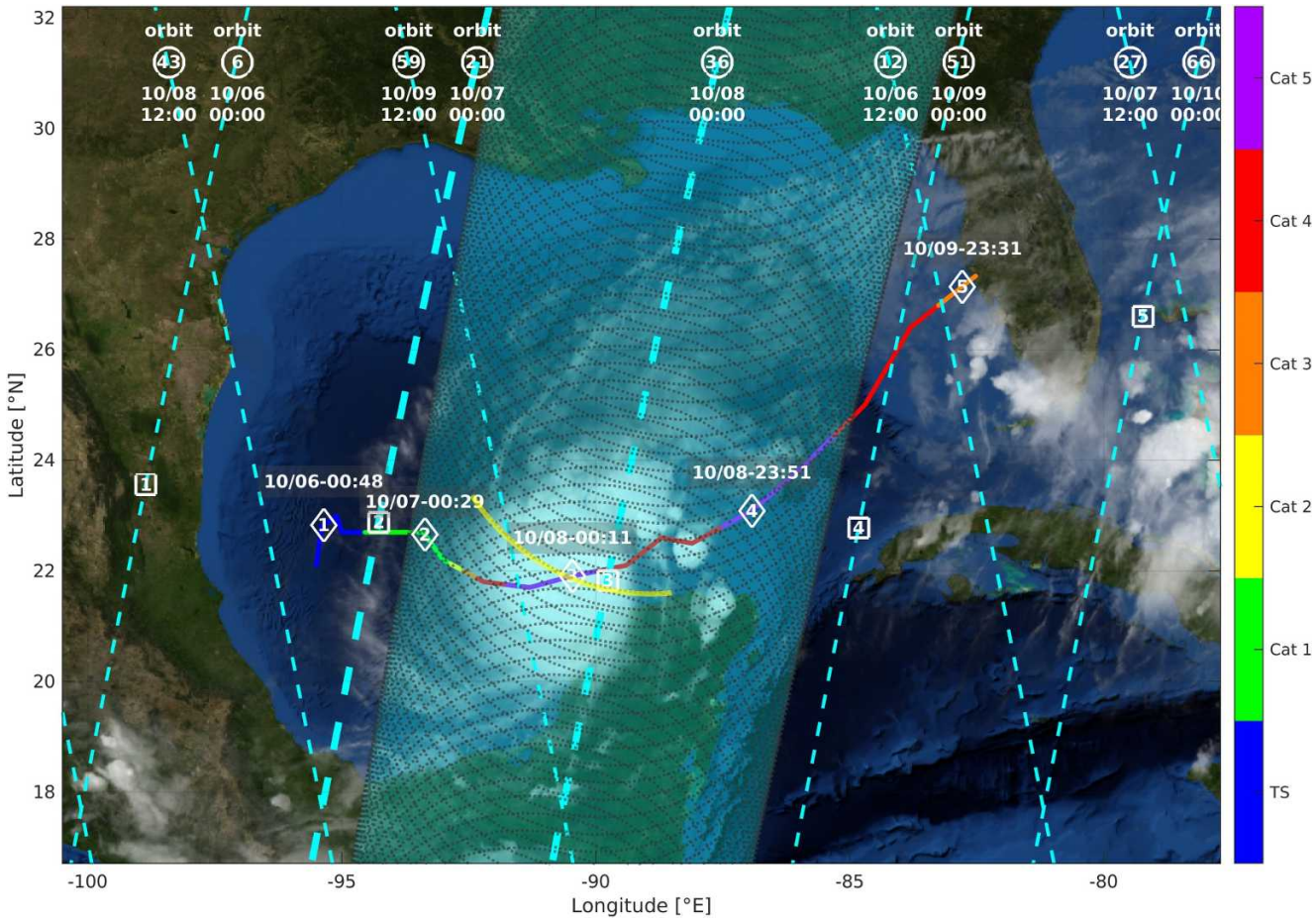

Figure 6. The path of Hurricane Milton from 10/06/2024 to 10/10/2024 with its color-coded intensity, as reconstructed by NOAA. The nine WIVERN satellite ground-tracks passing through the Gulf of Mexico during these 4 days are indicated with cyan dashed lines. Five orbits pass within 400 km from the hurricane center with the five positions of the hurricane eye and the closest satellite ground-track indicated by diamonds and squares, respectively. The WIVERN scanning pattern is shown only for the 10/08 descending pass, with the sector of the scan plotted in Figure 7 highlighted in yellow. Note that the overpasses (2 and 3) (thick dashed lines) are only 24 hr apart.

In Figure 7 an overview of the WIVERN measurements and products is plotted for a section of the scan passing near the cyclone eye (located at a distance along the scanning track around 350 km), highlighted in yellow for overpass with label (3) in Figure 6. Note the freezing level at around 5 km altitude, the shallow rain cells at the beginning of the scan and that the echo tops in the left portion of the eyewall appear to be greater than 15 km whereas, further along-track, the right portion of the eyewall is a couple of kilometer shallower (likely the result of less wind shear and to a stronger convection on the left side of the eyewall for this particular cross-cut).

In the three columns, from left to right, the evolution of the simulated quantities from Figure 7 is represented: the three most relevant WRF model quantities, the three main Level-1 observables and an example of three retrieved Level-2 products. In panels (a), (b) and (c), a cross-section of the eye and eyewall of the cyclone is clearly identifiable. The eye appears as a column of generally low hydrometeor contents with near-zero wind speed, while the eyewall and rainbands exhibit high total water content, leading to significant attenuation and eventually total extinction of the measured reflectivity signal (Z_m). Shallow convection cells can also be seen at the beginning of the scan, on the left of the plots. As expected, at altitudes above ~5 km (roughly the freezing level), Z_m generally correlates with IWC: extensive anvil clouds with high ice content are evident from panel (c), while at lower levels the rainbands outside of the eyewall are clearly visible with high content of hydrometeors. Panels (d), (e) and (f) highlight the dominance of horizontal winds in the Doppler velocity field, which exhibits the typical antisymmetric structure associated with cyclonic circulation, characterized by opposite wind directions on either side of the eye. In panel (g), convective updrafts (blue regions) are apparent within the eyewall, while below the

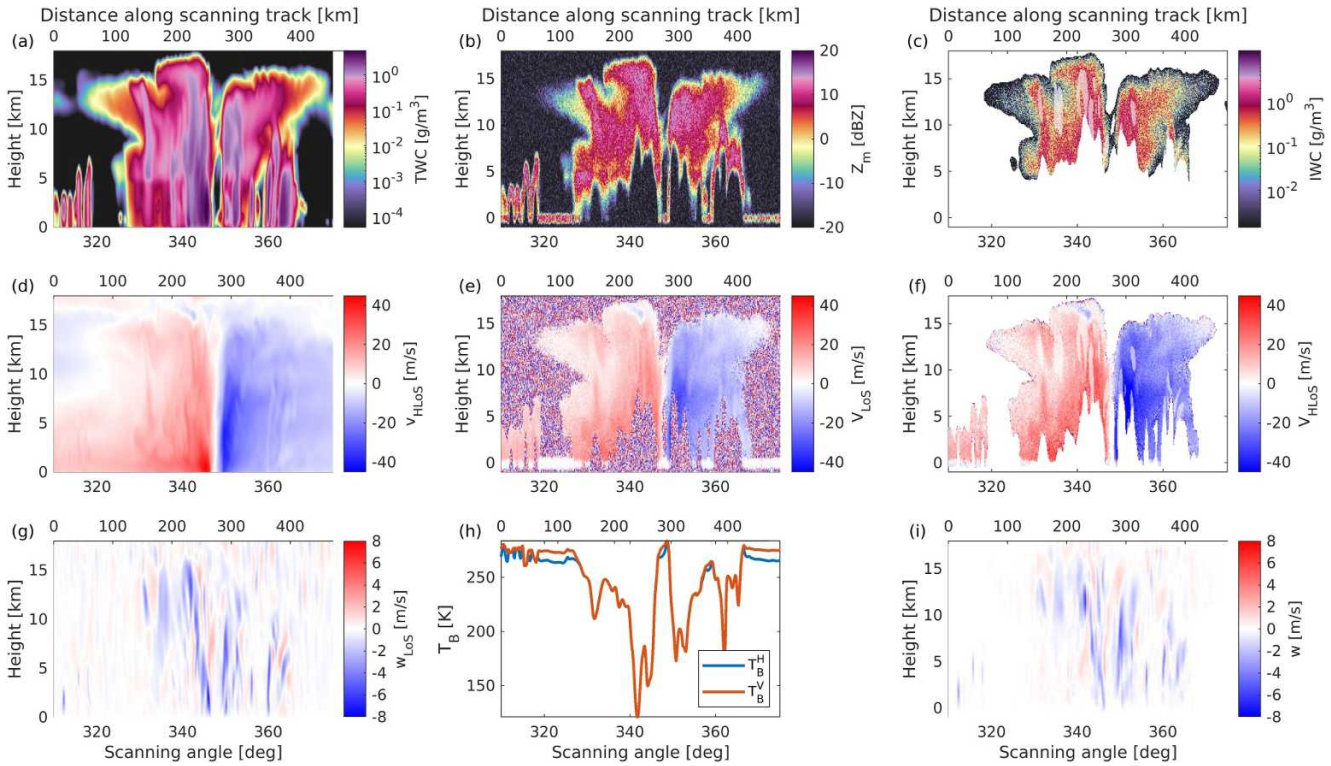

Figure 7. Curtain plots for the scan sector highlighted in yellow in Figure 6. The top row column shows: (a) antenna-weighted total water content (TWC), (b) measured reflectivity (Z_m) and (c) Level-2 retrieved Ice Water Content (IWC). The center row presents: (d) antenna-weighted horizontal component of the line-of-sight (LoS) wind (V_{HLoS}), (e) measured Doppler velocity (V_{LoS}) and (f) Level-2 retrieved horizontal wind (V_{HLoS}). The third row shows: (g) antenna-weighted vertical LoS wind component, (h) measured vertical and horizontal brightness temperatures (T_B^H and T_B^V) and (i) Level-2 neural-network predicted vertical wind (w_{pred}). In panels (c, f) regions identified as "convective" are semi-transparent.

freezing level. Regions of deep convection typically correspond to lower brightness temperatures, as seen in panel (h) in correspondence of the eyewall, rainbands and minor shallow convection cells. Panel (i) shows an example of the reconstruction of the vertical winds through a neural-network driven algorithm trained over a database of WIVERN simulations over hurricane Milton.

2.3. WIVERN Scanning Pattern

WIVERN scanning pattern is a distinctive feature of the mission, offering several advantages (Figure 8).

- The swath width is about 800 km, unprecedented for cloud and precipitation radars. The TRMM/GPM radars have swaths up to 250 km, with no sensitivity to clouds and their footprints are larger than 4 km. The INCUS mission will have a 10 km swath, but with similarly limited sensitivity to clouds and footprints close to 4 km. Cloudsat/EarthCARE CPR have much narrower swaths of 1.6 km and 750 m, respectively. WIVERN effectively bridges the gap between the km-scale resolution (footprint size) and mesocale coverage (swath width).
- Moving at about 500 km s^{-1}, the footprint sweeps through an unprecedented volume of the atmosphere. With a sampled area of about 500 km^{2}s^{-1}, it has unparalleled sampling capabilities. In comparison, EarthCARE and CloudSat CPR sample the troposphere sweeping areas at rates of 5.5 and 11 km^{2}s^{-1}, respectively, while the INCUS mission achieves 70 km^{2}s^{-1}. In short, in 1 week, WIVERN will sample as many cloudy columns as EarthCARE does in a year, and INCUS in 7 weeks.
- WIVERN measurements have azimuthal diversity, a critical feature for retrieving vector winds (i.e., the zonal and meridional components), depending on their location within the swath. As shown in Figure 8, the blue and red cells near the satellite ground track and at the edges of the swath have limited azimuthal diversity; accordingly, good retrievals are expected primarily for the along-track and cross-track components,

10.1029/2025EA004680

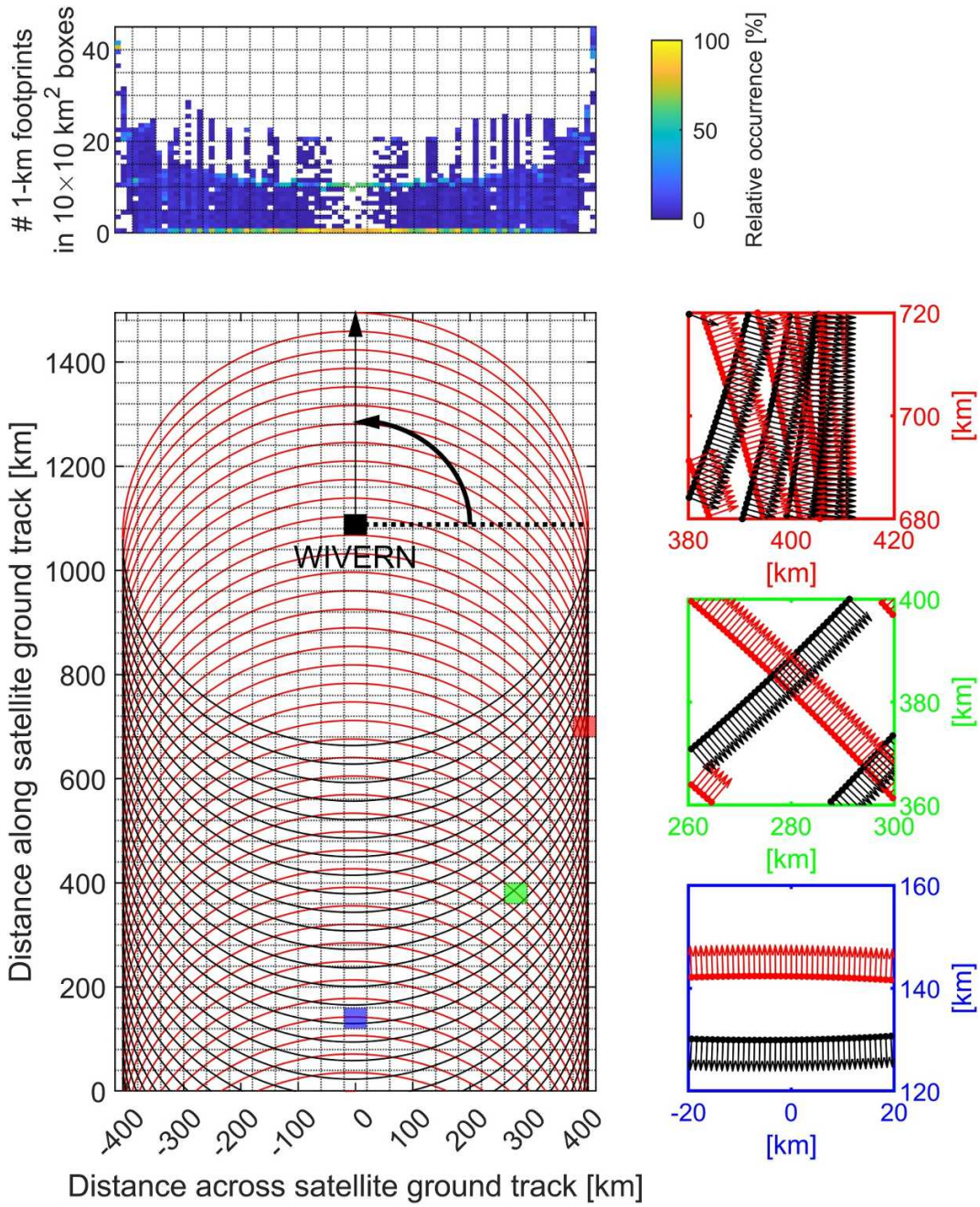

Figure 8. WIVERN scanning measurements at a fixed altitude. The satellite is assumed to move upward at 7.0 km s^{-1} while scanning an 800 km swath at 12 rpm. The radar footprint is about 1 km. Red and black dots indicate forward and backward views, respectively. The three insets on the right show zoomed-in views of the sampling within the green, cyan and pink cells, each covering a 40×40 km^2 region located at the swath edge and center. Red (black) arrows represent the HLoS directions for each available measurement in the cell for the forward (backward) views. The top inset shows the relative occurrence of 1 km along-track averaged measurements in each 10 $\times$ 10 km^2 pixel as a function of distance from the ground track.

respectively. In contrast, the green cell is characterized by looks with a wide range of azimuth angles, allowing the reconstruction of the horizontal wind vector.

- The number of 1 km along-track measurements in each 10 $\times$ 10 km^2 pixel is much higher near the edges of the swath than in the center, with a very sharp gradient in the 50 km closest to the swath edge (upper inset in

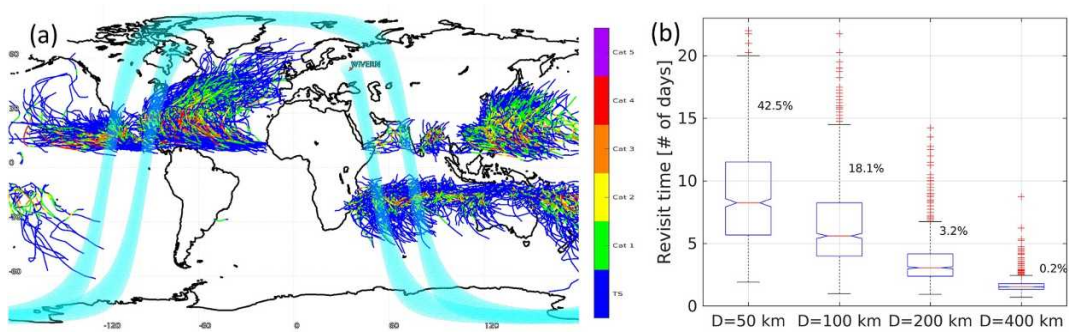

Figure 9. Panel (a): ground-tracks of the last 35 years TC that reached at least Category 1 level (maximum velocity above 33 m/s) during their lifetime (Knapp et al., 2010). The color for the tracks indicate different TC intensities (blue for tropical storm; green, yellow, orange, red, violet for TC from category 1 to category 5, respectively. Panel (b): revisit time (expressed in number of days) for the WIVERN ground-track to pass within a given distance (D) from the TC eye. In each boxplot, the central mark indicates the median, the bottom and top edges of the box the 25th and 75th percentiles, respectively. The whiskers indicate the range of non outliers whereas outliers are shown as "+" symbols. The percentage numbers express the probability of missing completely the TC.

Figure 8). In the central part of the swath, the distribution is bimodal, with either no measurements or about 10. This reflects the sparseness of the scans in this region.

On the other hand, near the swath edges, within a 20 km wide strip, the sampling is excellent, each 10×10 km^2 pixel contains between 20 and 56 measurements. This almost full coverage at the swath edges will allow to use WIVERN as a calibrating reference system for other sensors.

The sparse WIVERN sampling can be used to produce two swath products:

1. A three-dimensional Horizontal Wind Vector Field, which contains the reconstructed three-dimensional horizontal wind field across the full swath with a resolution of $10 \times 10 \times 0.5$ km^3 (Section 2.4).
2. A three-dimensional Stratiform Ice Mass Field, which contains the three-dimensional distribution of the ice mass also at a resolution of $10 \times 10 \times 0.5$ km^3 (Section 2.5).

2.3.1. WIVERN Tropical Cyclone Sampling

A systematic analysis has been conducted to assess how well WIVERN will sample the lifecycle of TCs. Statistics based on more than 1,350 tracks extracted from the database of the last 35 years TCs reaching at least Category 1 (i.e., 64 knots, Knapp et al. (2010); Figure 9a) coupled with simulations of the WIVERN orbit have been exploited to compute the distribution of the mean revisit time within a certain distance D from the TC eye for TCs lasting at least 3 days (99% of them). Results are presented in Figure 9b in the form of boxplots for four values of D from 50 to 400 km. The study reveals that 1.55 is the median (1.35 and 1.8 are the 25th and 75th percentiles) number of days required for the WIVERN track to revisit a TC within a 400 km distance from the TC center (fourth boxplot in Figure 9b). This guarantees that WIVERN will be able to map winds inside at least half of each TC more frequently than every other day. Note that only 0.2% of the TC are completely missed. In comparison, a nadir-pointing radar (like CloudSat or EarthCARE) would typically provide only a 2D curtain within 50 km of the eye every 8.3 days (5.7 and 11.5 are the 25th and 75th percentiles of the distribution, first boxplot in Figure 9b) and would miss the TC 42.5% of the time.

Finally note that with an average of about 42 TCs per year of Category 1 or more there will be on average about 17, 36 and 290 overpasses per year of a polar orbiting satellite like WIVERN within 25, 50 and 400 km, respectively. This is equivalent of having hundreds of TC dedicated field campaigns with aircrafts every year. When considering all TCs lasting at least 1 day (on average 102 per year), there will be on average about 32, 63 and 512 overpasses per year within 25, 50 and 400 km.

Tridon et al. (2023) exploited a large data set of TCs Tourville et al. (2015) as observed by CloudSat CPR to simulate WIVERN data by accounting for the increased attenuation introduced by the WIVERN slant observation geometry. They demonstrated that a slant looking 94 GHz radar with the expected WIVERN sensitivity (i.e., capable of measuring winds for target above −18 dBZ) will be able to observe a very large number of winds inside

TCs, particularly in the glaciated part of the storm above the freezing level. If we set the number of clouds detected by Cloudsat at any given level inside TCs to 100% as a touchstone, WIVERN Doppler velocity estimates will be more accurate than 3 m/s in over 50% of those clouds up to an altitude of around 11 km, with peak performance between 3 and 9 km. In TCs, this region is characterized by an abundance of clouds. Thanks to their low attenuation levels and good mass content, these clouds produce reflectivity signals with values above −20 dBZ, thus resulting in reliable Doppler estimates.

Since the footprints of WIVERN and CloudSat are similar (≈1 km wide) whereas the WIVERN footprint is moving at a velocity which is 70 times faster than the CloudSat one, WIVERN will sample a much larger area than CloudSat (and similarly EarthCARE). Therefore, when combining the sampling and sensitivity capabilities of the WIVERN and CloudSat radars, it is possible to conclude that inside TCs WIVERN will provide 30 times more accurate wind observations than CloudSat cloud observations. Overall it is expected that WIVERN will measure about 200 million precise wind measurements at 600 m vertical resolution and 10 km horizontal resolution within TCs per year.

The combination of these two findings reveals that WIVERN has significant potential for mapping TCs in three dimensions and monitoring their evolution, which can last for over a fortnight.

2.4. Three-Dimensional Horizontal Wind Vector Reconstruction

The three-dimensional horizontal wind vector field can be reconstructed using the WIVERN irregular sampling, through an inversion procedure (Battaglia et al., 2024; ESA WIVERN Team, 2025). The 2D horizontal wind field is recreated at different heights at grid points separated by 10×10 km^2. For each node, the two horizontal wind field components are found using an optimization technique based on the standard least squares method (Battaglia et al., 2024). The main idea is to minimize the error between the modeled LoS velocity and the available observations. The modeled LoS velocity is written in terms of the unknown horizontal wind velocity components. Observed data are weighted by an exponential drop based on the distance from the target and a correlation length. Due to sampling sparseness, the correlation length is 20 km near the ground track and decreases exponentially to 5 km at the edge where sampling is excellent. For each grid point, the problem reduces to a linear system, and its inversion allows for the determination of the horizontal components of the wind field by an analytic inverse procedure. Details are provided in Appendix A.

This retrieval procedure is limited by:

- Poor radar illumination (regions with no targets or clouds with radar reflectivity below the noise level of −18 dBZ);
- Presence of convective cells where the vertical wind component is not negligible;
- Azimuth diversity, as shown in Figure 8, which limits retrievals near the satellite ground track and at the edge of the swath.

2.5. Three-Dimensional Ice Mass Field Reconstruction

The reconstruction procedure is illustrated by taking a WIVERN acquisition for an ascending overpass on the 7th October with the satellite track passing in the vicinity of the eye. The model ice water path (IWP) with superimposed WIVERN scanning pattern is shown in the left panel of Figure 10. To estimate the three-dimensional ice mass distribution of cloud anvil from the WIVERN sampling, the WIVERN Level-2 IWC sparse retrieved points are first interpolated along each WIVERN ray at a fine vertical sampling of 100 m. Then the sparse points are gridded into a three-dimensional uniform grid with 100 m spacing in the vertical and at grid points separated by 10×10 km^2 (center panel in Figure 11). The same is done for the model outputs (left panel in Figure 11).

If multiple WIVERN measurements fall within the same grid box, the IWC attributed to the grid box is equal to the mean (in linear units) of the different IWC estimates. IWC values of 0 g/m^2 are attributed to grid boxes located above the cloud top height [that operationally could be derived from geostationary auxiliary measurements, for example, infrared brightness temperatures, whereas here are computed from the model output where the IWP exceeds 1 g/m^2 when computed from the top of the atmosphere downwards (panel in Figure 10)] and 500 m below the freezing level (assumed to be derived from auxiliary ECMWF reanalysis). The corresponding IWC field at 9.6 km is shown in the center panel of Figure 11. The WIVERN scanning pattern produces gaps, especially near

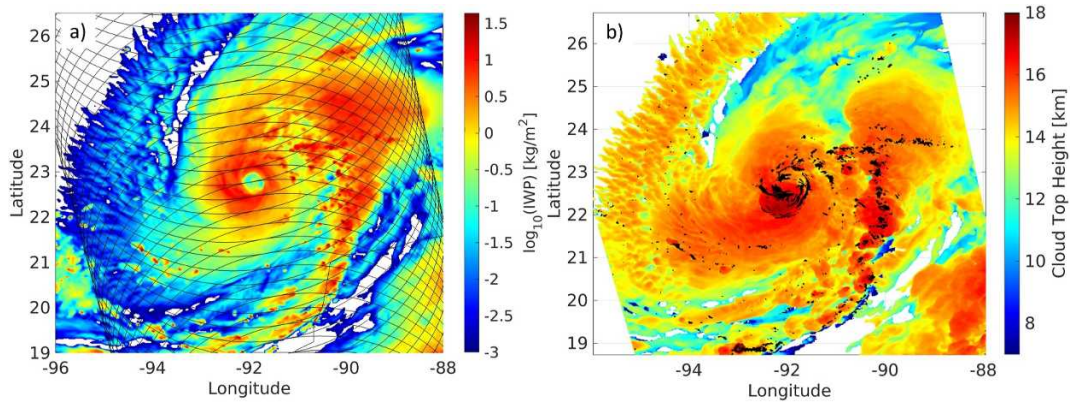

Figure 10. Left panel: WIVERN sampling for an overpass in proximity of the Milton eye on the 7th October at 11 UTC. The color is modulated by the ice water path (as indicated in the colorbar legend). Right panel: cloud top height, assumed to be detected from geostationary auxiliary data. Black areas correspond to convective columns where no IWC retrieval is attempted.

the satellite ground-track (see white pixel in the center panel of Figure 11). The grid points that are empty (because there is no WIVERN measurement falling inside the grid box) are filled by a fully three-dimensional interpolation procedure.

3. Results

The goal of this work is to demonstrate that WIVERN will be able to:

1. Provide a three-dimensional view of the horizontal wind inside TCs, in particular capturing the vertical wind shear, the upper level divergences and the in-cloud circulations inside the anvil produced by the hurricane convective towers, and some of the inflow and outflows in the lower layers of the atmosphere (1–2 km);
2. Identify the intensification of a TC by estimating the maximum winds in the inner core from close in time overpasses;
3. Profile the TC ice mass as a function of the distance from the eye, which will help in shedding light into the TC anvil formation and dissipation mechanisms.

The simulation of Hurricane Milton is used to demonstrate these features.

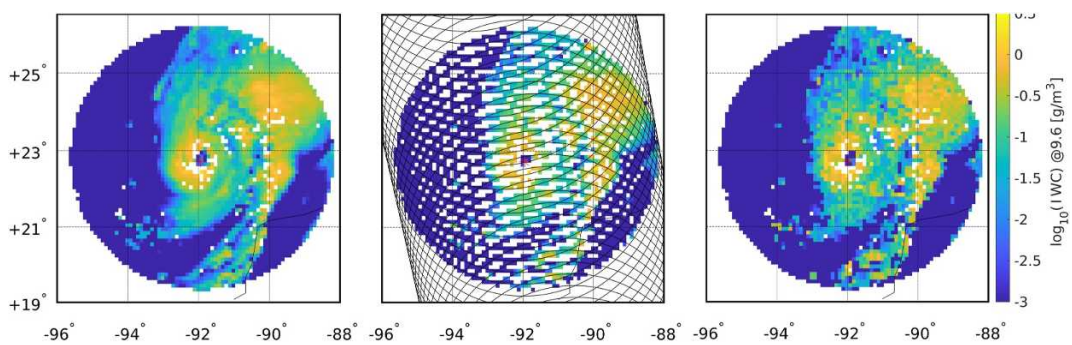

Figure 11. Reconstruction of the anvil IWC three-dimensional field from WIVERN measurements: horizontal cut at 9.6 km altitude for the case study shown in Figure 10. Results are shown only for a circular area of 400 km radius centered at the TC eye. Left panel: model $\log_{10}(IWC)$[g/m^3] (white pixels inside the 400 km radius correspond to convective towers where the retrieval is not attempted). Center panel: WIVERN Level-2 IWC gridded at 10×10 km^2 with the antenna boresight line of sight projected at the given height (black line). Right panel: WIVERN retrieved IWC after gap-filling is applied.

3.1. Tropical Cyclone Wind Shear Structure

The capability of the WIVERN mission to retrieve wind profiles within the hurricane's inner region and across multiple vertical layers allows for the reconstruction of radial wind patterns and provides new insights into the organization of the storm's inner-core circulation and wind shear distribution.

Thanks to its Doppler radar capabilities and its wide swath scanning, WIVERN can capture the storm internal circulation, particularly well in the glaciated part above 5 km. An overpass on 7 October at 12 UTC when Hurricane Milton was intensifying toward Category 3 status, corresponding to an ascending orbit with the right edge of the swath located approximately 150 km east to TC center (see Figure 12), is used to demonstrate the reconstruction of the three-dimensional horizontal wind field, via the technique described in Section 2.4. Figure 12 shows that the horizontal wind structure is accurately retrieved across the different vertical layers, clearly capturing the transition from the cyclonic circulation around the eye, still evident at around 7 km altitude (lower panels), to the divergent outflow at upper levels (top panel). Interestingly there is a good reconstruction even in the lowest layer at $H = 3$ km even if the coverage is limited (see density of white arrows in the bottom right panel). WIVERN is the only space-borne observing system potentially capable of resolving storm dynamics with this level of detail and spatial coverage. Such observations are crucial, for instance, to determine whether most of the mass detrained into the TC outflow originates from the eyewall or from the surrounding rainbands (Nolan et al., 2025).

To place the internal wind structure of the cyclone in the context of the surrounding large-scale environment, the storm is divided into four shear-relative quadrants (DL: downshear left, DR: downshear right, UL: upshear left, UR: upshear right), following the convention described by Matyas (2010); Rogers et al. (2015). This approach provides a consistent framework to analyze storm structure and convective organization under the influence of vertical wind shear. The classification is based on the direction of the environmental vertical wind shear, defined as the vector difference between winds at the 850 and 200 hPa pressure levels. The shear vector is computed within an annular region between 200 and 600 km from the cyclone center, thereby excluding the inner-core. This method captures the large-scale wind environment and helps interpret asymmetries in the cyclone structure, such as inflow and outflow patterns. Quadrant-based analysis has proven especially useful in characterizing precipitation asymmetries in sheared storms. In particular, rainfall tends to be concentrated in the downshear-left quadrant, where vertical motion and convective activity are typically strongest (Wingo & Cecil, 2010). Furthermore, recent studies have shown that asymmetries in the inner-core wind structure, shaped by vertical shear, play a crucial role in the onset and maintenance of rapid intensification. Convective bursts and vorticity maxima frequently develop in specific shear-relative regions, most notably in the downshear-left quadrant (B. Liu et al., 2022).

Figure 14 presents zonal (cyan line in Figure 13) and meridional (red line in Figure 13) vertical cuts through the TC eye. With the previous wind-shear classification, they correspond to four cuts in the middle of the UL, UR, DR and DL domains. In these vertical curtains it is possible to identify the radial inflows and outflows (here each cut is spanning a 400 km wide region). The two profiles display wind speed (left panel) and WIVERN-measured reflectivity (right panel), overlaid with both the modeled wind field (black vectors) and the retrieved wind vectors (red vectors). These radial profiles reveal the asymmetries typically found in tropical cyclones, both in terms of dynamic structure and hydrometeor distribution. Such asymmetries involve complex interactions between horizontal inflows and outflows, as well as convective regions characterized by intense updrafts and downdrafts (see arrows in the right panels of Figure 14). These reconstructions clearly demonstrate the potential of WIVERN measurements to shed light on the mechanisms driving the internal circulation of hurricanes, and therefore their organization and possible intensification.

3.1.1. Assessment of Wind Retrieval Errors

A statistical analysis of the error for the retrieved zonal and meridional components and the wind velocity is performed using 12 different scenes. The data set is filtered to remove points with an expected error greater than 10 m/s (for and estimation of the error see Appendix A). Outliers were then identified and excluded. Finally, a statistical analysis is performed on the filtered data set, clustering the results according to the distance from the satellite ground track (Figures 15 and 16). It is evident that the zonal component u has a larger error near the ground track where standard deviation errors can become larger than 8 m/s (this is due to the fact that, especially at low latitudes that component of the wind is only marginally affecting the LoS Doppler velocity measurement)

10.1029/2025EA004680

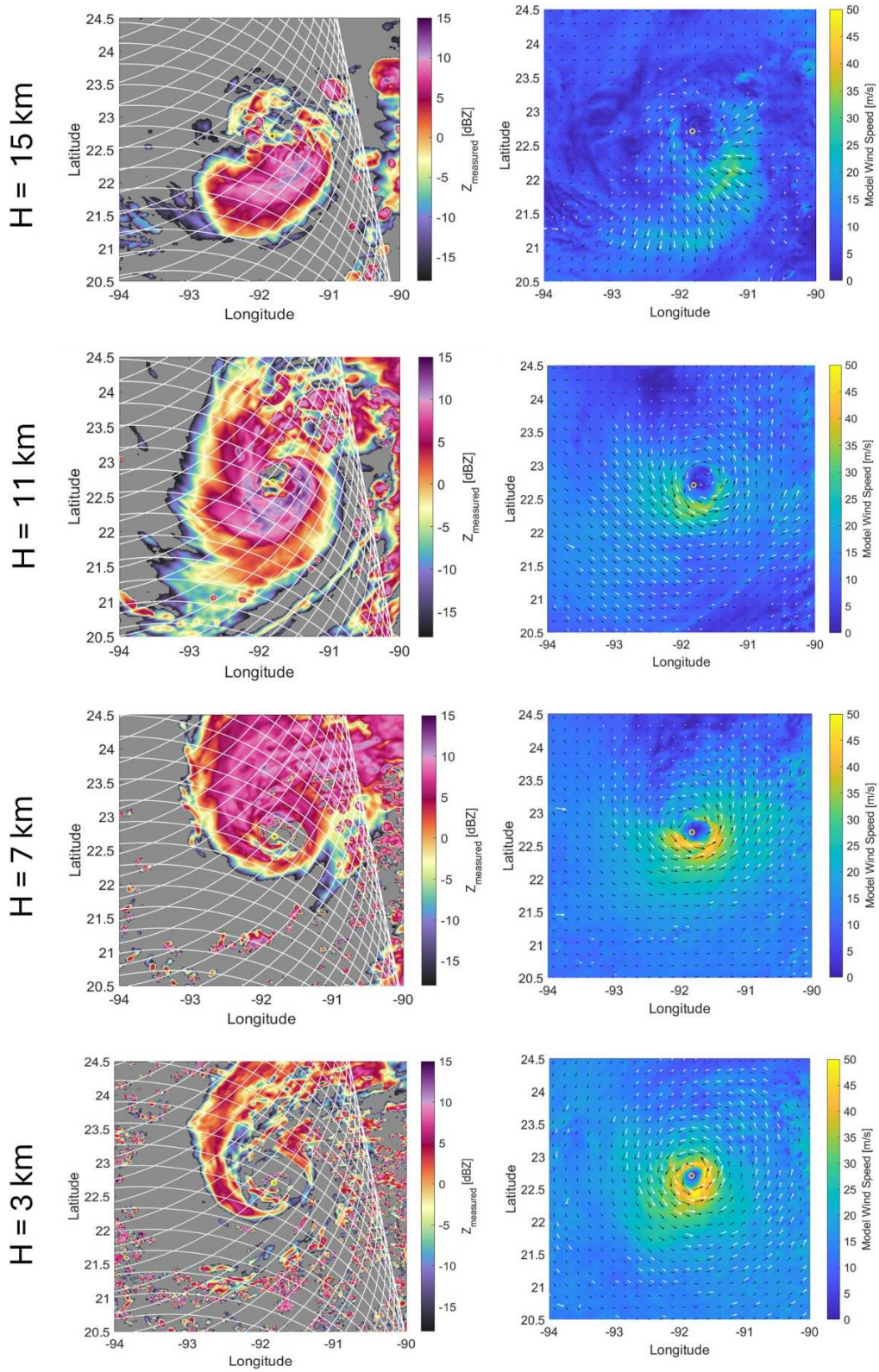

Figure 12. Example of three-dimensional reconstruction of the horizontal winds for Hurricane Milton simulated by the WRF model. Horizontal cross sections at four altitudes are considered: 15, 11, 7 and 3 km, respectively from top to bottom. Left columns: same-height horizontal cuts of simulated reflectivities in dBZ with the WIVERN scanning pattern superimposed. Right columns: model wind field (black vectors) with retrieved winds (white vectors). Note that the retrieved winds correspond to regions where clouds with good reflectivities are present.

whereas becomes lower than 2 m/s at ground track distances exceeding 150 km. The meridional component v on the other hand is characterized by a standard deviation n error which is typically smaller than 2 m/s (slightly worsening near the center and the edge). Overall in great part of the swath both the u and v estimates apper unbiased (this is a direct consequence of the conical scan, that tends to cancel out errors introduced by mispointing and non uniform beam filling, Battaglia, Rabino et al. (2025); Scarsi et al. (2024)).

As a result the overall horizontal wind magnitude (V_H) has larger uncertainty (up to 4.5 m/s) at the center of the swath (Figure 16). This is due to the lack of azimuth diversity in this areas, as explained in Section 2.3.

3.2. Tropical Cyclone Intensification

WIVERN will also be able to capture wind features inside the inner core of TCs. While W-band radars are typically limited by signal attenuation in regions with high liquid water content, the WIVERN slant view can enable penetration in regions heavily loaded with precipitation (e.g., the eyewall) from regions that are almost cloud-free (e.g., from the eye). Thanks to the multiple cross-cuts through the hurricane and reduced surface clutter (Coppola et al., 2025), it is possible to retrieve crucial information about the wind in the lower troposphere and inside the eyewall where the strongest winds occur. The horizontal wind vector swath product described in Section 2.4 can represent well the TC large-scale circulation, but its coarse resolution prevents an accurate representation of the dynamics in the presence of very strong horizontal variability of the wind that can exist close to the eye. For the wind structure near the eye a full reconstruction of the wind field can rely on a model; here the very simple one described by cyclostrophic balance as proposed by Holland (1980) is used. The azimuthal symmetric cyclostrophic tangential wind (V_c) can be written as:

$$V_c(r) = V_c(r_{\max}) \sqrt{\left(\frac{r_{\max}}{r}\right)^B e^{\left[1-\left(\frac{r_{\max}}{r}\right)^B\right]}} \tag{2}$$

where $r_{\max}$ is the radius of maximum wind and B is an non-dimensional parameter related to the maximum wind velocity by $V_c(r_{\max}) = \sqrt{B\,(p_n - p_c)/(\rho\, e)}$ where ρ is the air density, p_c and p_n are the central and ambient pressure, e is the Neper number.

The WIVERN measurements of the two successive overpasses, one before and one after the rapid intensification that occurred to Milton on 8 Oct 2024 (thick cyan lines labeled as 2 and 3 in Figure 6), are used to optimally fit the three free parameters of the model of Holland (1980) ($V_c(r_{\max})$, $r_{\max}$, B). An appropriate filtering process was applied to the measurements acquired at an altitude of 2 km, as presented in the top two panels of Figure 17. This included discarding data points where the reflectivity was below −18 dBZ, indicating an insufficient presence of hydrometeors to serve as tracers for wind estimation, or where the vertical velocity exceeded 2 m/s, typically associated with strong convective towers. Additionally, measurements with a Signal-to-Clutter Ratio (SCR) below 20 dB were excluded, as they indicate contamination of the Doppler signal by surface contributions.

In this context, the WIVERN capability to measure LoS Doppler velocities from a slant view enables winds in otherwise inaccessible regions to be observed. The slanted geometry plays a key role in determining reflectivity measurements. This feature is well highlighted by the two middle panels of Figure 17, where the measured reflectivity derived from the hurricane model output (background) is compared to the one produced by the WIVERN simulator (colored circles on WIVERN white scanning track). In first approximation, when attenuated reflectivity is estimated from model data, each atmospheric column is treated independently as a purely vertical one-dimensional profile. The Path-Integrated Attenuation (PIA) is computed by integrating the extinction coefficient vertically, and then subtracted from the unattenuated model reflectivity (accounting for the slant geometry with an amplification factor equal to $1/\cos(\theta_I) \approx 1.34$) to obtain a first approximation attenuated reflectivity. However, this simplification does not take into account the actual path followed by the radar pulse when propagating though the atmosphere. In contrast, the WIVERN simulator accounts for the true three-dimensional propagation of the radar beam along its slant path. It simulates how the signal interacts with the volume of atmosphere it traverses, thus properly capturing attenuation effects. Consequently, differences between the model-derived and simulator-derived attenuated reflectivity fields can be attributed to three-dimensional effects, which will be particularly relevant in regions characterized by large spatial variability of the hydrometeor structures, thus of the PIA field. These are made evident in the lower panel of Figure 17, where the difference

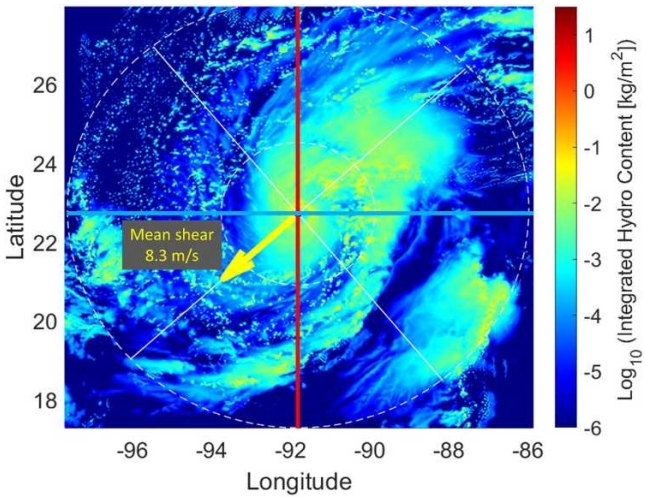

Figure 13. Example of shear-oriented quadrant division for the scene related to Hurricane Milton on 10/07/2024 at 12 UTC. The thin white lines divide the hurricane into four shear-relative quadrants, labeled with their respective acronyms: downshear left (DL), downshear right (DR), upshear left (UL), and upshear right (UR). The yellow arrow indicates the direction of the mean large-scale vertical wind shear vector, computed within the annular region between 200 and 600 km from the storm center, as delimited by the black dashed lines. The red and cyan thick lines represent radial cuts that cross the inner-core region of the tropical cyclone (shown in Figure 14).

between the two reflectivity estimates is superimposed on the PIA field, enabling the identification of areas where WIVERN slant-view geometry provides a clear advantage by avoiding heavily attenuating regions. A portion of the observation track, highlighted by the black rectangle in the left side panels of Figure 17, demonstrates this phenomenon. A zoomed-in view of this area is presented in Figure 18, where it is possible to distinguish two distinct scenarios. In the case of the red-colored circles, the reflectivity derived from the model exceeds that observed by WIVERN. This occurs because, in the layers above 2 km, the actual radar beam crosses the eyewall where strong attenuation strongly reduces the radar return. In contrast, the blue-colored circles correspond to observations where the radar beam penetrates from the eye, a region with relatively low attenuation. Here, WIVERN will measure reflectivity values that are higher than those expected from the model-1D approximation estimate, highlighting the radar ability to access regions typically inaccessible to conventional nadir-viewing systems. In summary, the WIVERN slant view is not always detrimental because of the increased slant attenuation. In deep convection, it sometimes allows penetrations into regions in the lower troposphere that are inaccessible by a W-band nadir-looking radar.

The WIVERN measurements are used to retrieve the three free parameters of Holland model through a least-squares fitting procedure using data acquired before and after the rapid intensification phase. The cost function minimization enables the selection of the optimal set of three parameters that best reproduce the cyclostrophic wind field within the first 70 km from the TC center. Figure 19 shows the azimuthal average around the TC eye of the horizontal winds as a function of the radial distance from the eye of the hurricane for the model outputs (circles) and obtained by using a least square best fitting procedure using WIVERN data before and after the rapid

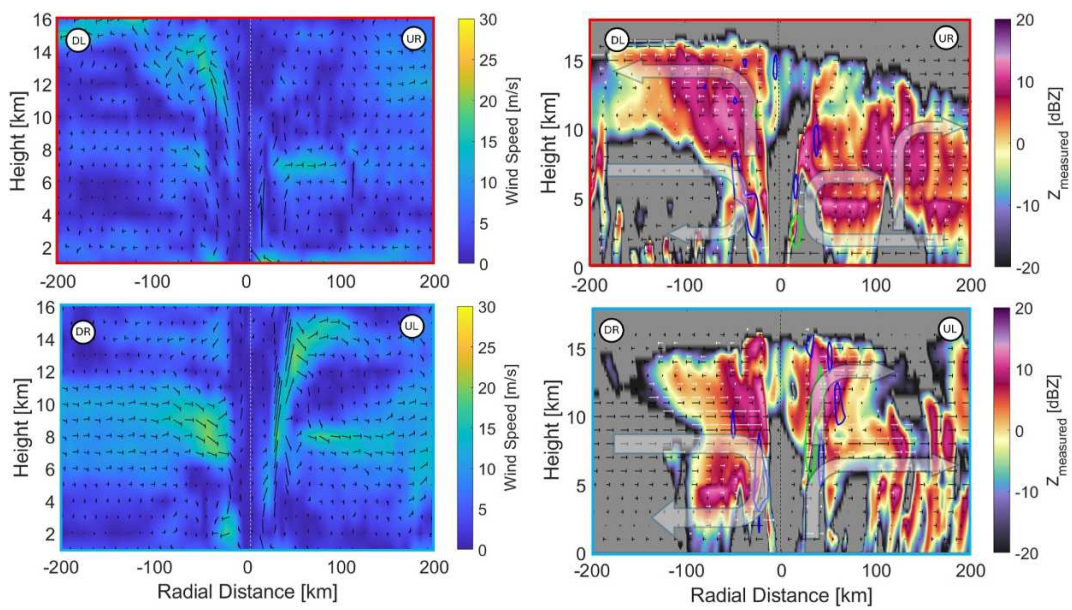

Figure 14. Meridional (top panels) and zonal (bottom panels) vertical cuts across the inner-core region of Hurricane Milton on 10/07/2024 at 12 UTC, each spanning 400 km through the storm center. Left panels show the model wind velocities projected onto the two vertical cuts (arrows) with their corresponding wind speed (color-coded). The right panels display WIVERN-measured reflectivity superimposed with the model horizontally projected radial wind velocities (black arrows) and those retrieved by WIVERN (white arrows) in correspondence to the scanning pattern shown in Figure 12. Mean circulations within each quadrant are shown by the large arrows. The contour lines highlight convective regions with blue contours corresponding to downdrafts of −1 m/s and green contours indicating updrafts of 3 m/s.

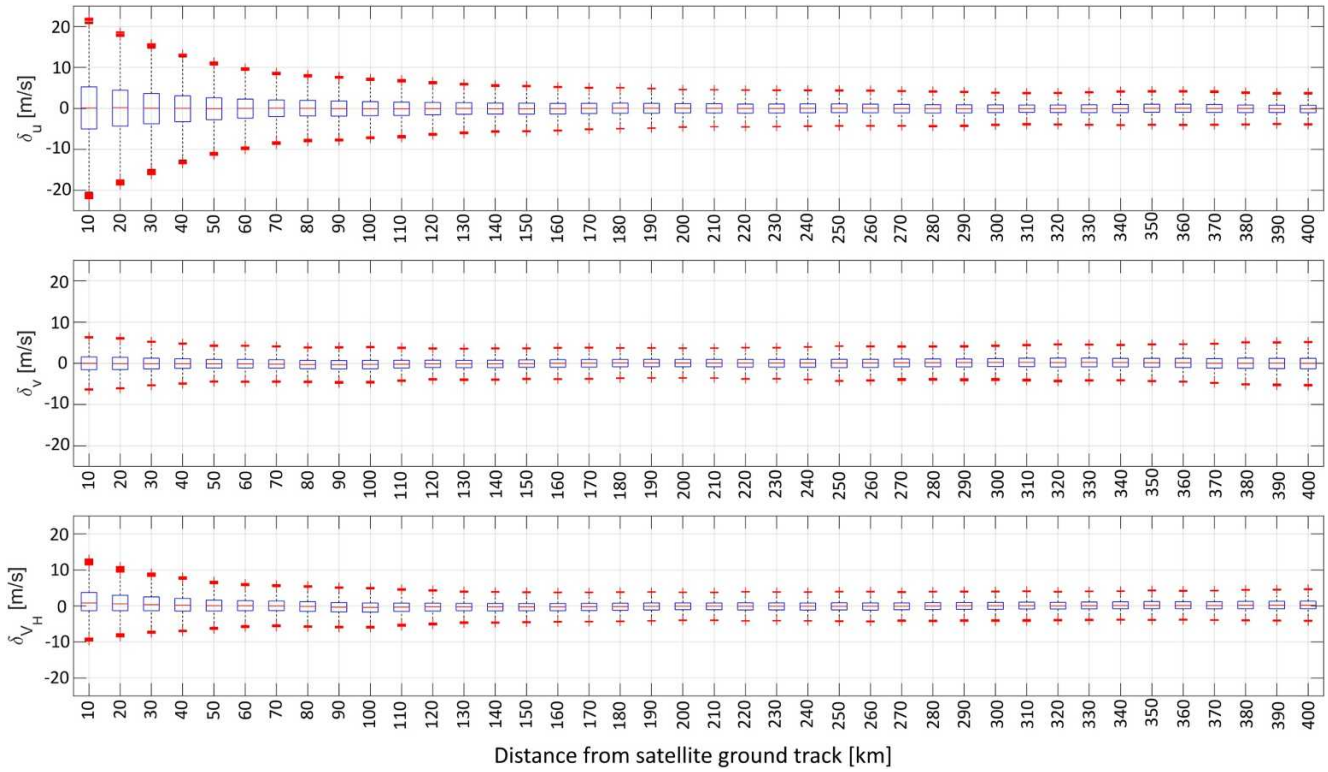

Figure 15. Error of the retrieved 3D horizontal wind velocity (δ_u on top, δ_v in the middle) and of the horizontal wind intensity δ_{V_H}, as a function of the track distance. The median is indicated by the central mark, and the bottom and top edges of the box represent the 25th and 75th percentiles, respectively. The whiskers show the range of non-outliers, while the "+" symbols represent the outliers.

intensification. As demonstrated in Figure 19 WIVERN measurements can properly capture the acceleration of winds from 30 to 60 m/s occurring in less than 24 hr. The retrieved parameters of the model proposed by Holland (1980) produce the thick continuous curves that are almost superimposed to the best-fit curves (thin dashed lines) of the azimuthally averaged wind speeds (circles). Note that more sophisticated models with more parameters (e.g., the model proposed by Willoughby et al. (2006) with 6 free parameters) could have been used but the scope here is just to showcase that WIVERN can peer into the hurricane wind inner structure.

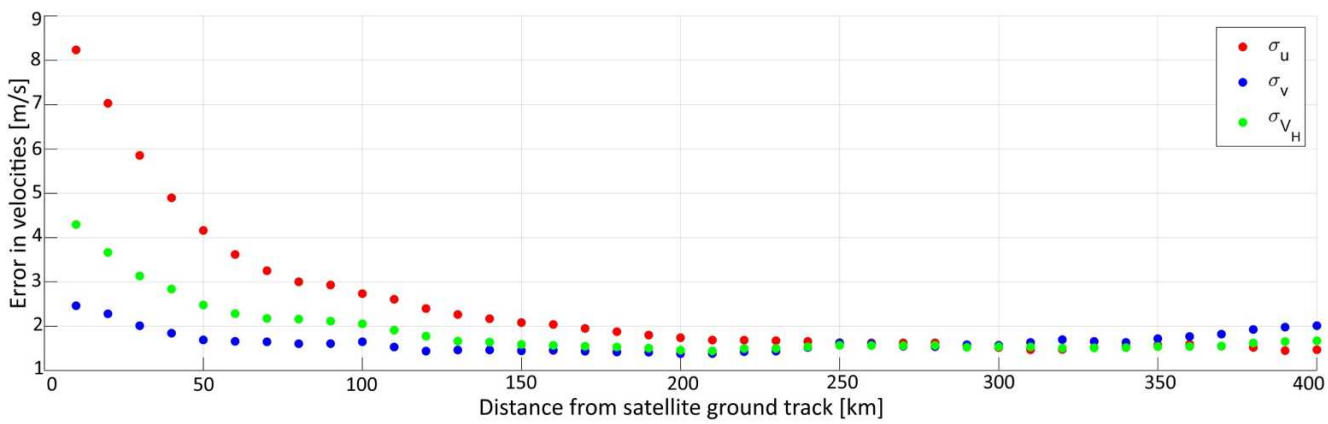

Figure 16. Standard deviation of the error of the zonal and meridional horizontal components u and v and of the horizontal intensity, V_H as a function of the distance from ground track.

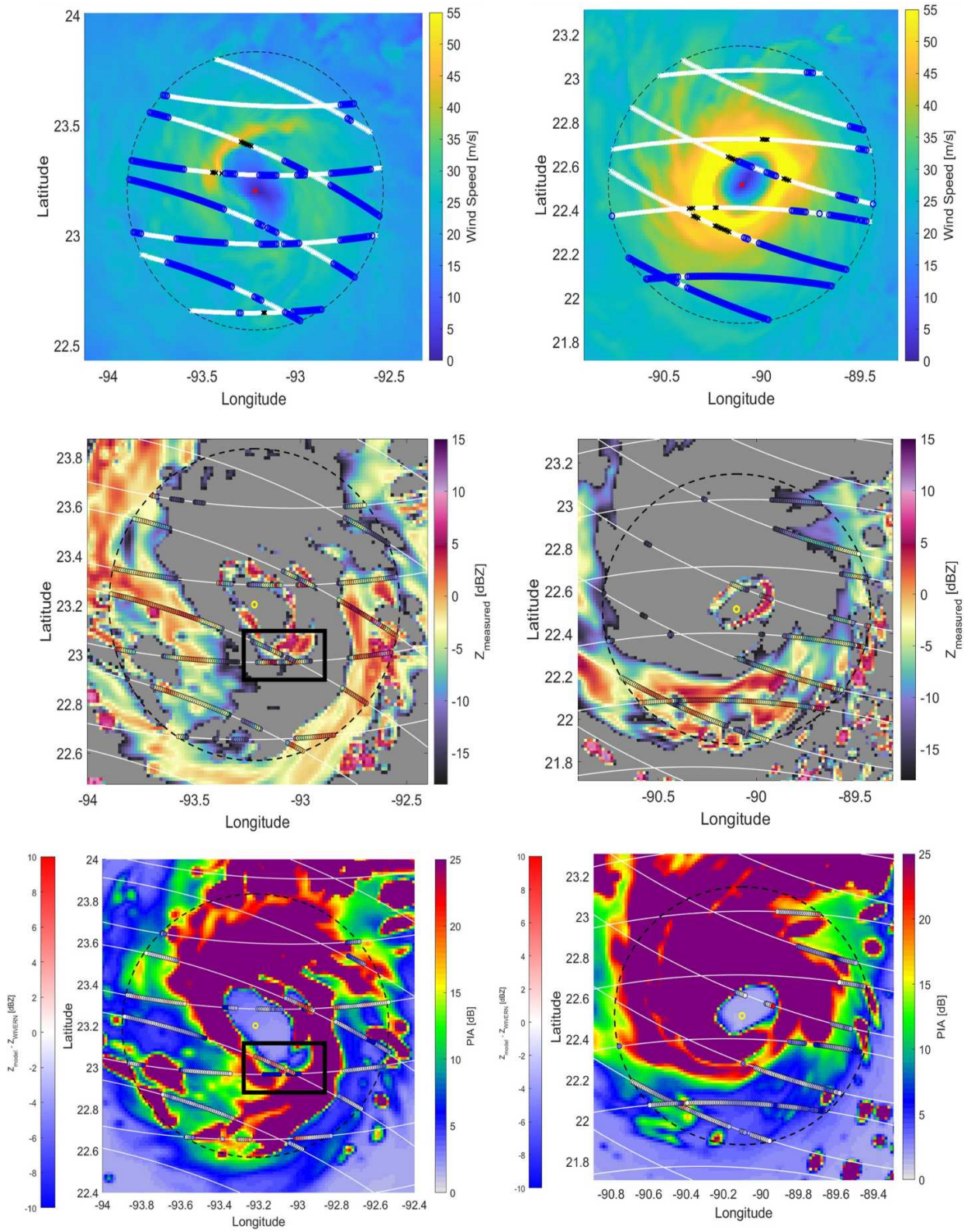

Figure 17.

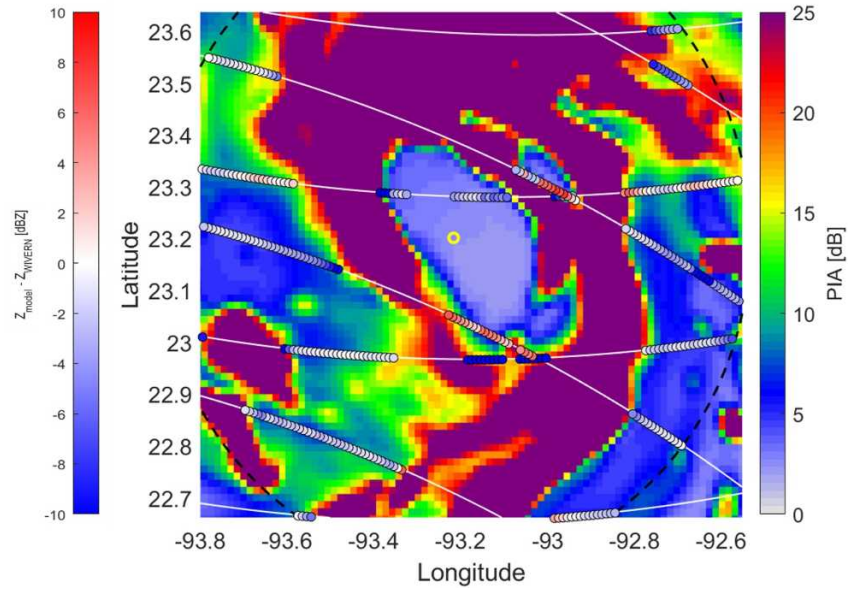

Figure 18. Zoomed-in view of the observation track segment highlighted in Figure 17.

This example demonstrates that WIVERN can provide insight in really extreme weather scenarios and that, thanks to its frequent overpasses over TCs, it can actually identify rapid intensification. Note that, in the best situation, two consecutive overpasses within 400 km can occur with one ascending and one descending orbit separated by 12 hr or with two ascending or two descending orbits separated by 24 hr (like in the previous example, orbits (2) and (3) in Figure 6).

3.3. Profiling Ice Mass

The WIVERN IWC retrieved with the methodology discussed in Section 2.5 can be accumulated to produce vertical distribution of the ice mass contents as a function of the distance from the TC eye. The results for the overpass shown in Figure 10 are depicted in Figure 20 with each annulus having a thickness of 10 km. Note that there is notably higher ice mass in the eyewall region compared to some of the outer rainband features. Eyewall's vertical velocities are dramatically stronger and more persistent than those in the outer rainbands (L. Wang et al., 2023). This affects microphysics along two lines:

- Stronger updrafts transport supercooled droplets and small ice particles to high altitudes, where temperatures are well below freezing level;
- Continuous recycling of particles (riming, aggregation, breakup, re-uptake) produces high concentrations of graupel, snow, and cloud ice.

As a result, the eyewall almost always shows larger total ice mass aloft, regardless of supercooled liquid water availability. Additionally, outer rainband convection tends to be more episodic and shallower on average than the ones in the eyewall and more mixed-phase dominant (D. Wu et al., 2021). The outer rainband region is also characterized by a substantial increase in ice mass toward the surface, which is consistent with several precipitation growth pathways that dominate in tropical rainbands. In priority order:

Figure 17. Inner core (i.e., distance from TC eye lower than 70 km as indicated by the black dashed circles) WIVERN sampling of Hurricane Milton at a 2 km altitude, before (left side) and after (right side) the rapid intensification occurred on 8 October 2024. Top panels: the scanning tracks of the antenna boresight are plotted above the two-dimensional hurricane horizontal wind speed field (color coded). WIVERN measurements discharged due to low reflectivity are marked with white crosses, those excluded due to high vertical wind velocity with black crosses, and valid measurements are indicated by blue circles. Middle panels: the model 1D-simulated reflectivity is colorcoded, while circles color-coded with the same color-bar along the WIVERN track represent WIVERN-measured reflectivity values accounting for the full three-dimensional geometry. Lower panels: PIA field of the two scenes with superimposed WIVERN track with colored circles color-coded with the color-bar on the left hand side representing the difference between the two aforementioned reflectivity values. The black rectangle in the left panels shows an interesting portion of track that is further analyzed in Figure 18.

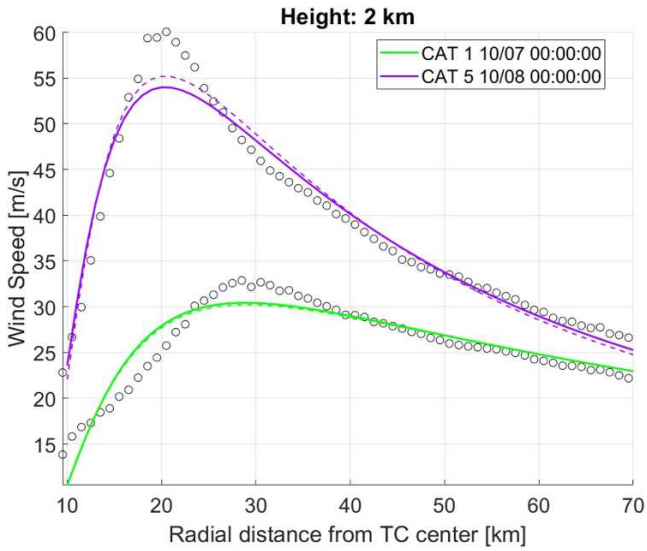

Figure 19. Wind inside hurricane Milton at 2 km height before and after the rapid intensification occurred on the 8 Oct 2024. Two descending orbits separated by 24 hr have been used (thick cyan lines in Figure 6). The true azimuthally averaged winds are plotted with circles with maximum wind speeds of 32 m/s before and 60 m/s after intensification reached at 30 and 20 km from the TC center, respectively. WIVERN measurements well reproduce the model proposed by Holland (1980).

3.3.1. Riming and Graupel Formation Below the Freezing Level

As supercooled drops collide with falling snowflakes, then snow crystals rapidly accrete supercooled liquid water, thus resulting in graupel. Graupel formation tends to peak below or just above the freezing level, not aloft. Since outer rainbands have significant amount of supercooled liquid water, riming is inherently very efficient. All in all, this creates a region where ice mass increases downward as hydrometeors grow while falling.

3.3.2. Warm-Rain Processes Feeding Ice Growth

Outer rainbands often have strong warm-rain production (collision–coalescence) below the melting level. These large drops can be lofted briefly and frozen or freeze during descent in strong downdrafts.

These mechanisms are much less common in the eyewall, where most precipitation originates aloft in deep convective cores.

Overall there is a very good agreement between the model (left panel of Figure 20) and the WIVERN reconstructed IWC fields (center panel). Discrepancies caused by the WIVERN sensitivity threshold (5 mg/m^3) are found in regions of very low IWCs (e.g., near cloud top) and in regions closer than 30 km from the eye, where there is less available data due to the smaller sampling volume for each annulus and the exclusion of convective regions. These discrepancies are indicated by μ greater than 0.2 in absolute value in the right panel (i.e., multiplicative bias larger than a factor of 1.58).

A statistical analysis of the IWC retrieval performance is carried out by running multiple overpassess with different orbits corresponding to 39 different snapshots of hurricane Milton straddling the rapid intensification period between 10 UTC on 6 October and 00 UTC on 8 October. The errors in the retrieved IWC are computed for the 39 different scenes. The standard deviation and the mean of such errors is shown in Figure 21. Results demonstrate that the WIVERN estimates are generally unbiased (multiplicative bias typically lower than a factor of 1.25 ($|\mu| < 0.1$, left panel in Figure 21), with standard deviation lower than a factor of 1.25 ($|\sigma| < 0.1$, right panel in Figure 21) in regions where the most data points are available (from 50 km of distance from the eye, from the eyewall outwards).

4. Conclusions

WIVERN, selected by ESA as the Earth Explorer 11 mission, is poised to significantly enhance the global tropical cyclone (TC) observing system in a way that is unprecedented in both spatial coverage and resolution.

Using high-resolution simulations of Hurricane Milton as a testbed, this study demonstrates that WIVERN's conically scanning geometry and Doppler capability enable the three-dimensional sampling of both the ice mass vertical structure and the horizontal wind field across the entire extent of tropical cyclones. WIVERN's data can

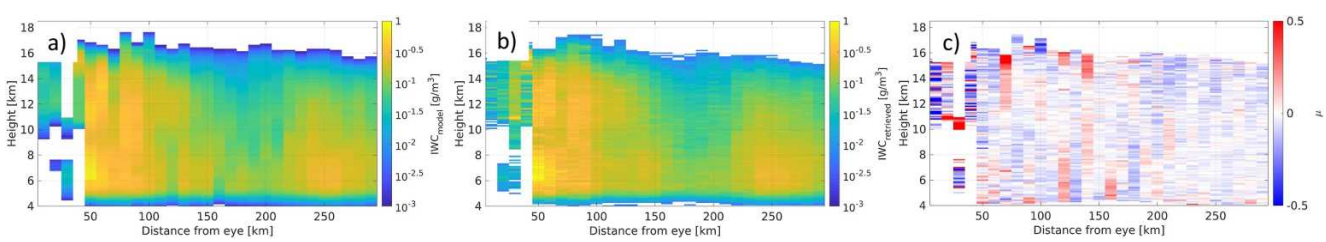

Figure 20. Vertical distribution of the ice mass contents (in g/m^3) as a function of the distance from the TC eye for the overpass shown in Figure 10 with the WRF model output (left) and reconstructed from a single WIVERN overpass (center panel). The right panel shows the bias $\mu \equiv \log_{10}(IWC_{retrieved}) - \log_{10}(IWC_{model})$ defined as the difference between the logarithmic values in base 10 of the WIVERN retrieved and the model mean IWC values.

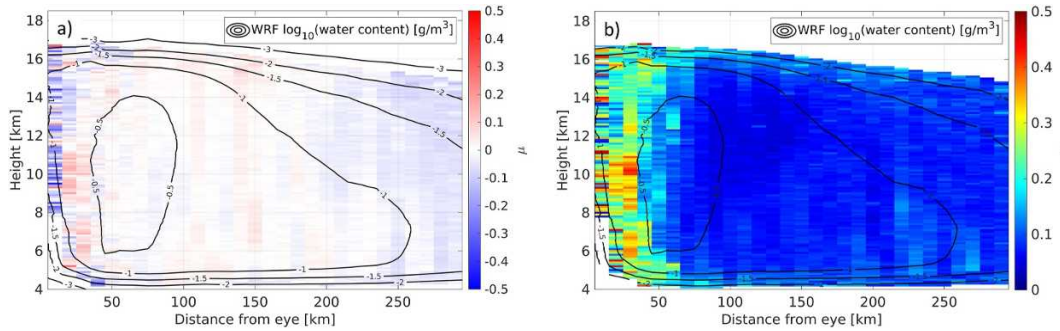

Figure 21. IWC retrieval performances: bias ($\mu \equiv \log_{10}(IWC_{retrieved}) - \log_{10}(IWC_{model})$, left panel) and standard deviation ($\sigma \equiv std\left[\log_{10}(IWC_{retrieved}) - \log_{10}(IWC_{model})\right]$, right panel) as a function of height and of the distance from the eye. Black lines correspond to contours of the mean values of the model $\log_{10}(IWC)$ distribution. Results are based on 39 different snapshots for Hurricane Milton from 10 UTC of 06/10 to 8 UTC of 07/10 with WIVERN orbits crossing the hurricane at different distances from the eye center (from 0 to 100 km).

be interpolated to produce gridded three-dimensional fields of ice mass and horizontal wind vectors at unrivaled vertical and horizontal resolutions.

Simulated overpasses of Hurricane Milton confirm that the Level-3 horizontal wind vector field products, derived directly from WIVERN's line-of-sight Doppler measurements, effectively reconstruct the storm's 3D horizontal wind structure. This capability is particularly evident in glaciated regions, where the products capture features such as vertical wind shear, upper-level divergence, and in-cloud circulations. Moreover, successive WIVERN overpasses—with a minimum revisit time of 12 hr under favorable orbital configurations—enable the monitoring of TC evolution, especially changes in wind intensity within the inner-core of the lower troposphere during periods of rapid intensification or weakening.

In addition to wind retrievals, WIVERN's radar reflectivity measurements support the estimation of the vertical distribution of ice mass. Although the system cannot detect ice water contents (IWCs) below 5 mg/m^3, it can identify the altitude and radial distance from the storm center where ice is detrained, and estimate its total mass.

The synergy between the Level-3 ice mass field and horizontal wind vector field products presents a unique opportunity to improve our understanding of TC dynamics, thermodynamics, and microphysics. In particular, this capability could help clarify key questions—such as whether the anvil ice mass originates primarily from the eyewall or from outer rainbands—and enhance insight into the coupling of latent heat release, circulation, and storm structure.

This study is limited to a simulation of a single hurricane (Milton) with a single model (WRF). Future work should aim to expand this study to include a broader set of simulated tropical cyclones (including typhoons) and/or to different cloud resolving models, in order to quantify expected retrieval errors for both wind and ice mass fields. Additionally, more advanced reconstruction techniques, including machine learning approaches, could be explored to further enhance the accuracy and utility of the derived gridded products. A dedicated analysis should also be conducted on convective regions to determine whether it is possible to measure the strength of convective motions and the extent to which the ice water content in such areas can be quantified.

Appendix A: Analytical Model for Vector Wind Inversions

Consider a region (covering the TC) where N_m measurements of the horizontal LoS velocity $\left((V_{HLoS})_i\ i = 1,\ldots,N_m\right)$ are collected. The domain is divided in N_c grid boxes with an area of 10×10 km^2 where a horizontal wind vector is sought after. For each node l, $l \in \{1,\ldots,N_c\}$, the minimization problem can be written as:

$$\min_{u_l,v_l} \quad \sum_{i=1}^{N_m}\left[\xi_i^{(l)}\left(\alpha_i u_l + \beta_i v_l - (V_{HLoS})_i\right)\right]^2, \tag{A1}$$

where N_m is the number of measurements, V_{HLoS} is the observed horizontal LoS velocity, $\alpha u_l + \beta v_l$ is the modeled V_{HLoS} written in terms of the unknown horizontal components (u and v), $\xi^{(l)}$ is an exponential weight and α and β are geometrical factors that accounts for the projection of the wind along the antenna boresight line of sight.

Solving the minimization expressed in Equation A1 is equivalent to invert the matrix equation:

$$\begin{bmatrix} \sum_{i=1}^{N_m} \alpha_i^2\, \xi_i^{(l)} & \sum_{i=1}^{N_m} \alpha_i\, \beta_i\, \xi_i^{(l)} \\ \sum_{i=1}^{N_m} \alpha_i\, \beta_i\, \xi_i^{(l)} & \sum_{i=1}^{N_m} \beta_i^2\, \xi_i^{(l)} \end{bmatrix} \begin{bmatrix} u_l \\ v_l \end{bmatrix} = \begin{bmatrix} \sum_{i=1}^{N_m} \alpha_i\, \xi_i^{(l)}\, (V_{HLoS})_i \\ \sum_{i=1}^{N_m} \beta_i\ \xi_i^{(l)}\, (V_{HLoS})_i \end{bmatrix} \tag{A2}$$

that allows to find u_l and v_l.

The quantity $\xi_i^{(l)} = \exp\left[-\left(r_i^{(l)}/L\right)^2\right]$ is a Gaussian weight, which ensure that measurements closer to the grid point contribute more significantly to the retrieve processing: $r_i^{(l)}$ is the distance between each measurement i and the grid point l, and $L > 0$ is a scaling parameter which accounts for the correlation length of the measurements. Larger values of L imply that the measurements are correlated over a wider area; conversely, smaller values of L indicate that the measurements have shorter spatial correlation.

The errors can be estimated using the standard error propagation from Equation A2 and considering that the horizontal wind intensity $V_{H,l} = \sqrt{u_l^2 + v_l^2}$:

$$\delta u_l = \frac{1}{|\det(\mathcal{A}_l)|} \sqrt{\sum_{i=1}^{N_m} \left(\xi_i^{(l)} \delta V_{HLoS,i} \sum_{j=1}^{N_m} \beta_j\, \xi_j \left(\alpha_i \beta_j - \alpha_j \beta_i\right) \right)^2} \tag{A3}$$

$$\delta v_l = \frac{1}{|\det(\mathcal{A}_l)|} \sqrt{\sum_{i=1}^{N_m} \left(\xi_i^{(l)} \delta V_{HLoS,i} \sum_{j=1}^{N_m} \alpha_j\, \xi_j \left(\alpha_j \beta_i - \alpha_i \beta_j\right) \right)^2} \tag{A4}$$

$$\delta V_{H,l} = \frac{\sqrt{A + B - 2C}}{V_{H,l} |\det(\mathcal{A}_l)|} \tag{A5}$$

$$\begin{cases} A = \left(\sum_{i=1}^{N_m} \beta_i\, \xi_i^{(l)} \left(u_l \beta_i - v_l \alpha_i\right) \right)^2 \sum_{i=1}^{N_m} \left(\alpha_i\, \xi_i^{(l)} \delta V_{HLoS,i} \right)^2 \\ B = \left(\sum_{i=1}^{N_m} \alpha_i\, \xi_i^{(l)} \left(u_l \beta_i - v_l \alpha_i\right) \right)^2 \sum_{i=1}^{N_m} \left(\beta_i\, \xi_i^{(l)} \delta V_{HLoS,i} \right)^2 \\ C = \left(\sum_{i=1}^{N_m} \beta_i\, \xi_i^{(l)} \left(u_l \beta_i - v_l \alpha_i\right) \right) \left(\sum_{i=1}^{N_m} \alpha_i\, \xi_i^{(l)} \left(u_l \beta_i - v_l \alpha_i\right) \right) \times \\ \qquad \times \sum_{i=1}^{N_m} \alpha_i \beta_i \left(\xi_i^{(l)} \delta V_{HLoS,i} \right)^2 \end{cases} \tag{A6}$$

where $\mathcal{A}_l$ denotes the matrix on the left-hand side of Equation A2.

Conflict of Interest

The authors declare no conflicts of interest relevant to this study.

Availability Statement

The data of the WRF simulation outputs for Hurricane Milton, as well as the corresponding WIVERN simulation data sets generated under different observational conditions, used for visualization of the main observables, analysis of the rapid intensification, and reconstruction of Level-3 products (ice water content and winds 3D field), are available at Figshare via https://doi.org/10.6084/m9.figshare.30038245 or https://figshare.com/s/4e378b4520820c004d1a, with CC-BY-4.0 license (Manconi, 2025).

Acknowledgments
This research has been supported by the European Space Agency under the activities "WInd VElocity Radar Nephoscope (WIVERN) Phase A Science and Requirements Consolidation Study" (ESA Contract Number RFP/3–18420/24/NL/IB/ab). The work by Battaglia, Manconi and Coppola have been carried out within the Space It Up project funded by the Italian Space Agency (ASI) and the Ministry of University and Research (MUR) under contract no. 2024-5-E.0–CUP no. I53D24000060005 This work used the Mafalda and Felipe High Performance Computing Facilities at Politecnico di Torino. Open access publishing facilitated by Politecnico di Torino, as part of the Wiley - CRUI-CARE agreement.

References

Avenas, A., Mouche, A., Tandeo, P., Piolle, J.-F., Chavas, D., Fablet, R., et al. (2023). Reexamining the estimation of tropical cyclone radius of maximum wind from outer size with an extensive synthetic aperture radar data set. *Monthly Weather Review*, *151*(12), 3169–3189. https://doi.org/10.1175/MWR-D-23-0119.1

Battaglia, A., Cambiotti, C., Carbone, A. F., & Da Silva, S. (2024). Reconstruction of the horizontal wind field inside weather systems from the sparse sampling envisaged for the wind velocity radar nephoscope (WIVERN) mission. In *IGARSS 2024–2024 IEEE international geoscience and remote sensing symposium* (pp. 8925–8927). https://doi.org/10.1109/IGARSS53475.2024.10640420

Battaglia, A., Kollias, P., Dhillon, R., Roy, R., Tanelli, S., Lamer, K., et al. (2020). Spaceborne cloud and precipitation radars: Status, challenges, and ways forward. *Reviews of Geophysics*, *58*(3), e2019RG000686. https://doi.org/10.1029/2019RG000686

Battaglia, A., Martire, P., Caubet, E., Phalippou, L., Stesina, F., Kollias, P., & Illingworth, A. (2022). Observation error analysis for the wind velocity radar nephoscope w-band Doppler conically scanning spaceborne radar via end-to-end simulations. *Atmospheric Measurement Techniques*, *15*(9), 3011–3030. https://doi.org/10.5194/amt-15-3011-2022

Battaglia, A., Rabino, R., Mroz, K., Tridon, F., & Parodi, A. (2025). Non uniform beam filling correction for the Doppler velocity measured by the WIVERN conically scanning radar. *Journal of Atmospheric and Oceanic Technology*. https://doi.org/10.1175/JTECH-D-25-0050.1

Battaglia, A., Rizik, A., Sikaneta, I., & Tridon, F. (2025). I and Qs simulation and processing envisaged for spaceborne polarization diversity Doppler radars. *IEEE Transactions on Geoscience and Remote Sensing*, *63*, 1–14. https://doi.org/10.1109/TGRS.2025.3529672

Benjamin, S. G., Grell, G. A., Brown, J. M., Smirnova, T. G., & Bleck, R. (2004). Mesoscale weather prediction with the RUC hybrid isentropic–terrain-following coordinate model. *Monthly Weather Review*, *132*(2), 473–494. https://doi.org/10.1175/1520-0493(2004)132<0473:mwpwtr>2.0.co;2

Brauer, N. S., Kirstetter, P. E., Basara, J. B., Hristova-Veleva, S., Tanelli, S., & Joseph Turk, F. (2024). Precipitation microphysics in tropical cyclones: A global perspective using the NASA global precipitation measurement mission dual-frequency precipitation radar. *Journal of Geophysical Research: Atmospheres*, *129*(1), e2023JD038709. https://doi.org/10.1029/2023JD038709

Cecil, D. J., Zipser, E. J., & Nesbitt, S. W. (2002). Reflectivity, ice scattering, and lightning characteristics of hurricane eyewalls and rainbands. Part I: Quantitative description. *Monthly Weather Review*, *130*(4), 769–784. https://doi.org/10.1175/1520-0493(2002)130⟨0769:RISALC⟩2.0.CO;2

Coppola, M., Battaglia, A., Tridon, F., & Kollias, P. (2025). Improved hydrometeor detection near the Earth's surface by a conically scanning spaceborne W-band radar. *EGUsphere, 2025*, 1–24. https://doi.org/10.5194/egusphere-2025-416

Emanuel, K. (2001). Contribution of tropical cyclones to meridional heat transport by the oceans. *Journal of Geophysical Research*, *106*(D14), 14771–14781. https://doi.org/10.1029/2000JD900641

Emanuel, K. (2003). Tropical cyclones. *Annual Review of Earth and Planetary Sciences*, *31*(1), 75–104. https://doi.org/10.1146/annurev.earth.31.100901.141259

Emanuel, K. (2018). 100 years of progress in tropical cyclone research. *Meteorological Monographs*, *59*, 15.1–15.68. https://doi.org/10.1175/AMSMONOGRAPHS-D-18-0016.1

Emanuel, K., Desautels, C., Holloway, C., & Korty, R. (2004). Environmental control of tropical cyclone intensity. *Journal of the Atmospheric Sciences*, *61*(7), 843–858. https://doi.org/10.1175/1520-0469(2004)061⟨0843:ECOTCI⟩2.0.CO;2

ESA WIVERN Team. (2025). *Report for mission selection: Earth explorer 11 candidate mission Wivern*. (Tech. Rep.). ESA-EOPSM-WIVE-RP-4798. https://doi.org/10.5281/zenodo.15607041

Fiori, E., Ferraris, L., Molini, L., Siccardi, F., Kranzlmueller, D., & Parodi, A. (2017). Triggering and evolution of a deep convective system in the Mediterranean Sea: Modelling and observations at a very fine scale. *Quarterly Journal of the Royal Meteorological Society*, *143*(703), 927–941. https://doi.org/10.1002/qj.2977

Fiori, E., Parodi, A., & Siccardi, F. (2010). Turbulence closure parameterization and grid spacing effects in simulated supercell storms. *Journal of the Atmospheric Sciences*, *67*(12), 3870–3890. https://doi.org/10.1175/2010jas3359.1

Fiori, E., Parodi, A., & Siccardi, F. (2011). Uncertainty in prediction of deep moist convective processes: Turbulence parameterizations, microphysics and grid-scale effects. *Atmospheric Research*, *100*(4), 447–456. https://doi.org/10.1016/j.atmosres.2010.10.003

Frank, & Ritchie (2001). Effects of vertical wind shear on the intensity and structure of numerically simulated hurricanes. *American Meteorological Society*, 2249–2269. https://doi.org/10.1175/1520-0493(2001)129⟨2249:EOVWSO⟩2.0.CO;2

Gill, D., Michalakes, J., Dudhia, J., Skamarock, W., & Gopalakrishnan, S. (2004). Nesting in WRF 2.0. In *Wrf/mm5 joint workshop* (pp. 22–25).

Hasan, M. B., Guimond, S. R., Yu, M., Reddy, S., & Giraldo, F. X. (2022). The effects of numerical dissipation on hurricane rapid intensification with observational heating. *Journal of Advances in Modeling Earth Systems*, *14*(8), e2021MS002897. https://doi.org/10.1029/2021ms002897

Hence, D. A., & Houze, R. A. (2011). Vertical structure of hurricane eyewalls as seen by the TRMM precipitation radar. *Journal of the Atmospheric Sciences*, *68*(8), 1637–1652. https://doi.org/10.1175/2011JAS3578.1

Hence, D. A., & Houze, R. A. (2012). Vertical structure of tropical cyclones with concentric eyewalls as seen by the TRMM precipitation Radar. *Journal of the Atmospheric Sciences*, *69*(3), 1021–1036. https://doi.org/10.1175/JAS-D-11-0119.1

Hendricks, E. A., Peng, M. S., Fu, B., & Li, T. (2010). Quantifying environmental control on tropical cyclone intensity change. *Monthly Weather Review*, *138*(8), 3243–3271. https://doi.org/10.1175/2010MWR3185.1

Hersbach, H., Bell, B., Berrisford, P., Hirahara, S., Horányi, A., Muñoz-Sabater, J., et al. (2020). The Era5 global reanalysis. *Quarterly Journal of the Royal Meteorological Society*, *146*(730), 1999–2049. https://doi.org/10.1002/qj.3803

Holbach, H. M., Bousquet, O., Bucci, L., Chang, P., Cione, J., Ditchek, S., et al. (2023). Recent advancements in aircraft and in situ observations of tropical cyclones. *Tropical Cyclone Research and Review*, *12*(2), 81–99. https://doi.org/10.1016/j.tcrr.2023.06.001

Holland, G. J. (1980). An analytic model of the wind and pressure profiles in hurricanes. *Monthly Weather Review*, *108*(8), 1212–1218. https://doi.org/10.1175/1520-0493(1980)108⟨1212:AAMOTW⟩2.0.CO;2

Houze, R. A. (2010). Clouds in tropical cyclones. *Monthly Weather Review*, *138*(2), 293–344. https://doi.org/10.1175/2009MWR2989.1

Huang, H., & Chen, F. (2019). Precipitation microphysics of tropical cyclones over the Western North Pacific based on GPM DPR observations: A preliminary analysis. *Journal of Geophysical Research: Atmospheres*, *124*(6), 3124–3142. https://doi.org/10.1029/2018JD029454

Iacono, M. J., Delamere, J. S., Mlawer, E. J., Shephard, M. W., Clough, S. A., & Collins, W. D. (2008). Radiative forcing by long-lived greenhouse gases: Calculations with the AER radiative transfer models. *Journal of Geophysical Research*, *113*(D13). https://doi.org/10.1029/2008jd009944

Illingworth, A. J., Battaglia, A., Bradford, J., Forsythe, M., Joe, P., Kollias, P., et al. (2018). WIVERN: A new satellite concept to provide global In-Cloud winds, precipitation, and cloud properties. *Bulletin of the American Meteorological Society*, *99*(8), 1669–1687. https://doi.org/10.1175/BAMS-D-16-0047.1

Judt, F., & Chen, S. S. (2016). Predictability and dynamics of tropical cyclone rapid intensification deduced from high-resolution stochastic ensembles. *Monthly Weather Review*, *144*(11), 4395–4420. https://doi.org/10.1175/mwr-d-15-0413.1

Kalesse, H., & Kollias, P. (2013). Climatology of high cloud dynamics using profiling ARM Doppler Radar observations. *Journal of Climate*, *26*(17), 6340–6359. https://doi.org/10.1175/JCLI-D-12-00695.1

Kaplan, J., & DeMaria, M. (2003). Large-scale characteristics of rapidly intensifying tropical cyclones in the North Atlantic basin. *Weather and Forecasting*, *18*(6), 1093–1108. https://doi.org/10.1175/1520-0434(2003)018⟨1093:LCORIT⟩2.0.CO;2

Klotzbach, P. J., Bowen, S. G., Pielke, R., & Bell, M. (2018). Continental U.S. Hurricane landfall frequency and associated damage: Observations and future risks. *Bulletin of the American Meteorological Society*, *99*(7), 1359–1376. https://doi.org/10.1175/BAMS-D-17-0184.1

Knapp, K. R., Kruk, M. C., Levinson, D. H., Diamond, H. J., & Neumann, C. J. (2010). The international best track archive for climate stewardship (IBTRACS): Unifying tropical cyclone data. *Bulletin of the American Meteorological Society*, *91*(3), 363–376. https://doi.org/10.1175/2009BAMS2755.1

Kollias, P., Puidgomènech Treserras, B., Battaglia, A., Borque, P. C., & Tatarevic, A. (2023). Processing reflectivity and Doppler velocity from Earthcare's cloud-profiling radar: The c-FMR, c-cd and c-apc products. *Atmospheric Measurement Techniques*, *16*(7), 1901–1914. https://doi.org/10.5194/amt-16-1901-2023

Lagasio, M., Fagugli, G., Ferraris, L., Fiori, E., Gabellani, S., Masi, R., et al. (2022). A complete Meteo/Hydro/Hydraulic chain application to support early warning and monitoring systems: The Apollo Medicane use case. *Remote Sensing*, *14*(24), 6348. https://doi.org/10.3390/rs14246348

Lee, T.-Y., & Wing, A. A. (2024). Satellite-based estimation of the role of cloud-radiative interaction in accelerating tropical cyclone development. *Journal of the Atmospheric Sciences*, *81*(6), 959–982. https://doi.org/10.1175/JAS-D-23-0142.1

Liu, B., Wang, M., & Zhao, K. (2022). Asymmetric inner-core structure and its impact on rapid intensification of a sheared tropical cyclone. *Frontiers in Earth Science*, *10*, 871540. https://doi.org/10.3389/feart.2022.871540

Liu, Y., Guan, S., Lin, I.-I., Zhao, W., Jin, F.-F., Liu, P., & Tian, J. (2025). Storm size modulates tropical cyclone intensification through an Oceanic pathway in global oceans. *Journal of Climate*, *38*(4), 891–908. https://doi.org/10.1175/JCLI-D-24-0398.1

Manconi, F. (2025). WIVERN tropical cyclone studies—Hurricane Milton case study. https://doi.org/10.6084/m9.figshare.30038245.v4

Manconi, F., Battaglia, A., & Kollias, P. (2025). Characterization of surface clutter signal in the presence of orography for a spaceborne conically scanning W-band Doppler radar. *Atmospheric Measurement Techniques*, *18*(10), 2295–2310. https://doi.org/10.5194/amt-18-2295-2025

Marchand, R., Mace, G. G., Ackerman, T., & Stephens, G. (2008). Hydrometeor detection using Cloudsat—An Earth-orbiting 94-GHz cloud radar. *Journal of Atmospheric and Oceanic Technology*, *25*(4), 519–533. https://doi.org/10.1175/2007JTECHA1006.1

Matyas, C. J. (2010). Locating convection in Landfalling tropical cyclones: A GIS-based analysis of radar reflectivities and comparison to lightning-based observations. *Physical Geography*, *31*(5), 385–406. https://doi.org/10.2747/0272-3646.31.5.385

Mouche, A., Chapron, B., Knaff, J., Zhao, Y., Zhang, B., & Combot, C. (2019). Copolarized and cross-polarized SAR measurements for high-resolution description of major hurricane wind structures: Application to IRMA category 5 Hurricane. *Journal of Geophysical Research: Oceans*, *124*(6), 3905–3922. https://doi.org/10.1029/2019JC015056

Mustich, F., Battaglia, A., Manconi, F., Kollias, P., & Parodi, A. (2025). Convective–stratiform identification neural network (CONSTRAINN) for the WIVERN mission. *Remote Sensing*, *17*(15), 2590. https://doi.org/10.3390/rs17152590

Nolan, D. S., Fischer, M. S., & O'Neill, M. E. (2025). Reconsideration of the mass and condensate sources for the tropical cyclone outflow. *Bulletin of the American Meteorological Society*, *106*(7), E1342–E1359. BAMS-D-24-0284.1. https://doi.org/10.1175/BAMS-D-24-0284.1

Nolan, D. S., & Rappin, E. D. (2008). Increased sensitivity of tropical cyclogenesis to wind shear in higher SST environments. *Geophysical Research Letters*, *35*(14). https://doi.org/10.1029/2008GL034147

Ou, Y., Wu, Z., Xie, Y., & Xiang, Q. (2025). Distinct outflow dynamics and cloud properties in rapidly intensifying tropical cyclones. *Geophysical Research Letters*, *52*(19), e2025GL118372. https://doi.org/10.1029/2025GL118372

Porcacchia, L., Kirstetter, P.-E., Maggioni, V., & Tanelli, S. (2019). Investigating the GPM dual-frequency precipitation radar signatures of low-level precipitation enhancement. *Quarterly Journal of the Royal Meteorological Society*, *145*(724), 3161–3174. https://doi.org/10.1002/qj.3611

Powers, J. G., Klemp, J. B., Skamarock, W. C., Davis, C. A., Dudhia, J., Gill, D. O., et al. (2017). The weather research and forecasting model: Overview, system efforts, and future directions. *Bulletin of the American Meteorological Society*, *98*(8), 1717–1737. https://doi.org/10.1175/bams-d-15-00308.1

Protat, A., Delanoë, J., Bouniol, D., Heymsfield, A. J., Bansemer, A., & Brown, P. (2007). Evaluation of ice water content retrievals from cloud radar reflectivity and temperature using a large airborne in situ microphysical database. *Journal of Applied Meteorology and Climatology*, *46*(5), 557–572. https://doi.org/10.1175/JAM2488.1

Protat, A., & Williams, C. R. (2011). Assessment of CloudSat reflectivity measurements and ice cloud properties using ground-based and airborne cloud radar observations. *Journal of Applied Meteorology and Climatology*, *50*, 2120–2138.

Ricciardulli, L., Howell, B., Jackson, C. R., Hawkins, J., Courtney, J., Stoffelen, A., et al. (2023). Remote sensing and analysis of tropical cyclones: Current and emerging satellite sensors. *Tropical Cyclone Research and Review*, *12*(4), 267–293. https://doi.org/10.1016/j.tcrr.2023.12.003

Rios-Berrios, R., Finocchio, P. M., Alland, J. J., Chen, X., Fischer, M. S., Stevenson, S. N., & Tao, D. (2024). A review of the interactions between tropical cyclones and environmental vertical wind shear. *Journal of the Atmospheric Sciences*, *81*(4), 713–741. https://doi.org/10.1175/JAS-D-23-0022.1

Rizik, A., Battaglia, A., Tridon, F., Scarsi, F. E., Kötsche, A., Kalesse-Los, H., et al. (2023). Impact of crosstalk on reflectivity and Doppler measurements for the WIVERN polarization diversity Doppler Radar. *IEEE Transactions on Geoscience and Remote Sensing*, *61*, 1–14. https://doi.org/10.1109/TGRS.2023.3320287

Rogers, R., Reasor, P., & Lorsolo, S. (2013). Airborne Doppler observations of the inner-core structural differences between intensifying and steady-state tropical cyclones. *Monthly Weather Review*, *141*(9), 2970–2991. https://doi.org/10.1175/MWR-D-12-00357.1

Rogers, R., Reasor, P., & Zhang, J. (2015). Multiscale structure and evolution of Hurricane Earl (2010) during rapid intensification. *Monthly Weather Review*, *143*(2), 536–562. https://doi.org/10.1175/MWR-D-14-00175.1

Scarsi, F. E., Battaglia, A., Tridon, F., Martire, P., Dhillon, R., & Illingworth, A. (2024). Mispointing characterization and Doppler velocity correction for the conically scanning Wivern Doppler radar. *Atmospheric Measurement Techniques*, *17*(2), 499–514. https://doi.org/10.5194/amt-17-499-2024

Schenkel, B. A., Edwards, R., & Coniglio, M. (2020). A climatological analysis of ambient deep-tropospheric vertical wind shear impacts upon tornadoes in tropical cyclones. *Weather and Forecasting*, *35*(5), 2033–2059. https://doi.org/10.1175/WAF-D-19-0220.1

Scoccimarro, E., Gualdi, S., Bellucci, A., Sanna, A., Fogli, P. G., Manzini, E., et al. (2011). Effects of tropical cyclones on ocean heat transport in a high-resolution coupled general circulation model. *Journal of Climate*, *24*(16), 4368–4384. https://doi.org/10.1175/2011JCLI4104.1

Skamarock, W. C., Klemp, J. B., Dudhia, J., Gill, D. O., Liu, Z., Berner, J., et al. (2019). A description of the advanced research WRF model version 4. *National Center for Atmospheric Research*, *145*(145), 550.

Smirnova, T. G., Brown, J. M., & Benjamin, S. G. (1997). Performance of different soil model configurations in simulating ground surface temperature and surface fluxes. *Monthly Weather Review*, *125*(8), 1870–1884. https://doi.org/10.1175/1520-0493(1997)125<1870:podsmc>2.0.co;2

Smirnova, T. G., Brown, J. M., Benjamin, S. G., & Kim, D. (2000). Parameterization of cold-season processes in the maps land-surface scheme. *Journal of Geophysical Research*, *105*(D3), 4077–4086. https://doi.org/10.1029/1999jd901047

Soci, C., Hersbach, H., Simmons, A., Poli, P., Bell, B., Berrisford, P., et al. (2024). The Era5 global reanalysis from 1940 to 2022. *Quarterly Journal of the Royal Meteorological Society*, *150*(764), 4014–4048. https://doi.org/10.1002/qj.4803

Subrahmanyam, K. V., Kumar, K. K., & Tourville, N. D. (2018). Cloudsat observations of three-dimensional distribution of cloud types in tropical cyclones. *IEEE Journal of Selected Topics in Applied Earth Observations and Remote Sensing*, *11*(2), 339–344. https://doi.org/10.1109/JSTARS.2017.2786666

Thatcher, L., & Pu, Z. (2011). How vertical wind shear affects tropical cyclone intensity change: An overview. In A. Lupo (Ed.), *Recent Hurricane research (chap. 13)*. IntechOpen. https://doi.org/10.5772/15416

Thompson, G., & Eidhammer, T. (2014). A study of aerosol impacts on clouds and precipitation development in a large winter cyclone. *Journal of the Atmospheric Sciences*, *71*(10), 3636–3658. https://doi.org/10.1175/jas-d-13-0305.1

Tourville, N., Stephens, G., DeMaria, M., & Vane, D. (2015). Remote sensing of tropical cyclones: Observations from cloudsat and a-train profilers. *Bulletin of the American Meteorological Society*, *96*(4), 609–622. https://doi.org/10.1175/BAMS-D-13-00282.1

Tridon, F., & Battaglia, A. (2015). Dual-frequency radar Doppler spectral retrieval of rain drop size distributions and entangled dynamics variables. *Journal of Geophysical Research: Atmospheres*, *120*(11), 5585–5601. https://doi.org/10.1002/2014JD023023

Tridon, F., Battaglia, A., Rizik, A., Scarsi, F. E., & Illingworth, A. (2023). Filling the gap of wind observations inside tropical cyclones. *Earth and Space Science*, *10*(11), e2023EA003099. https://doi.org/10.1029/2023EA003099

Turk, F. J., Ringerud, S. E., Camplani, A., Casella, D., Chase, R. J., Ebtehaj, A., et al. (2021). Applications of a Cloudsat-TRMM and Cloudsat-GPM satellite coincidence data set. *Remote Sensing*, *13*(12), 2264. https://doi.org/10.3390/rs13122264

Uma, K., & Reshma, B. (2024). Vertical structure of North Indian Ocean tropical cyclones: A composite analysis using TRMM and GPM. *Dynamics of Atmospheres and Oceans*, *105*, 101421. https://doi.org/10.1016/j.dynatmoce.2023.101421

Wadler, J. B., Cione, J. J., Zhang, J. A., Kalina, E. A., & Kaplan, J. (2022). The effects of environmental wind shear direction on tropical cyclone boundary layer thermodynamics and intensity change from multiple observational data sets. *Monthly Weather Review*, *150*(1), 115–134. https://doi.org/10.1175/MWR-D-21-0022.1

Wang, H., Zhao, D., Xu, H., Wang, Q., Liang, J., & Yen, T.-H. (2025). The role of wishe in the rapid intensification of super Typhoon Hinnamnor (2022). *Journal of Geophysical Research: Atmospheres*, *130*(1), e2024JD041864. https://doi.org/10.1029/2024JD041864

Wang, L., Bao, X., Hu, Y., Zhang, S., Lin, W., & Zhuang, Y. (2023). Microphysics of heavy rain associated with the eyewall and inner rainbands of Typhoon Meranti (2016). *Journal of Geophysical Research: Atmospheres*, *128*(22), e2022JD037288. https://doi.org/10.1029/2022JD037288

Willoughby, H. E., Darling, R. W. R., & Rahn, M. E. (2006). Parametric representation of the primary hurricane vortex. Part II: A new family of sectionally continuous profiles. *Monthly Weather Review*, *134*(4), 1102–1120. https://doi.org/10.1175/MWR3106.1

Wingo, M. T., & Cecil, D. J. (2010). Effects of vertical wind shear on tropical cyclone precipitation. *Monthly Weather Review*, *138*(3), 645–662. https://doi.org/10.1175/2009MWR2921.1

Wu, C.-C., Wu, S.-N., Wei, H.-H., & Abarca, S. F. (2016). The role of convective heating in tropical cyclone eyewall ring evolution. *Journal of the Atmospheric Sciences*, *73*(1), 319–330. https://doi.org/10.1175/JAS-D-15-0085.1

Wu, D., Zhang, F., Chen, X., Ryzhkov, A., Zhao, K., Kumjian, M. R., & Chan, P.-W. (2021a). Evaluation of microphysics schemes in tropical cyclones using polarimetric radar observations: Convective precipitation in an outer rainband. *Monthly Weather Review*, *149*(4), 1055–1068. https://doi.org/10.1175/MWR-D-19-0378.1

Wu, S.-N., & Soden, B. J. (2017). Signatures of tropical cyclone intensification in satellite measurements of ice and liquid water content. *Monthly Weather Review*, *145*(10), 4081–4091. https://doi.org/10.1175/MWR-D-17-0046.1

Wu, S.-N., Soden, B. J., & Alaka, G. J., Jr. (2020). Ice water content as a precursor to tropical cyclone rapid intensification. *Geophysical Research Letters*, *47*(21), e2020GL089669. https://doi.org/10.1029/2020GL089669

Wu, S.-N., Soden, B. J., & Nolan, D. S. (2021b). Examining the role of cloud radiative interactions in tropical cyclone development using satellite measurements and WRF simulations. *Geophysical Research Letters*, *48*(15), e2021GL093259. https://doi.org/10.1029/2021GL093259

Yurovskaya, M., Kudryavtsev, V., & Chapron, B. (2023). A self-similar description of the wave fields generated by tropical cyclones. *Ocean Modelling*, *183*, 102184. https://doi.org/10.1016/j.ocemod.2023.102184

Zagrodnik, J. P., & Jiang, H. (2014). Rainfall, convection, and latent heating distributions in rapidly intensifying tropical cyclones. *Journal of the Atmospheric Sciences*, *71*(8), 2789–2809. https://doi.org/10.1175/JAS-D-13-0314.1